# EXPLORING METHODS TO EXTRACT VERTICAL MOTIONS IN WINTER STORMS

BY

ANDREW ROSENOW

THESIS

Submitted in partial fulfillment of the requirements
for the degree of Master of Science in Atmospheric Sciences
in the Graduate College of the
University of Illinois at Urbana-Champaign, 2011

Urbana, Illinois

Adviser:

Professor Robert Rauber

**Abstract**

Methods of retrieving vertical motions in wintertime cyclones are tested for the 915 MHz profiler, a profiling radar on the University of Alabama-Huntsville Mobile Integrated Profiling System, used during several winter cyclones observed during the Profiling of Winter Storms (PLOWS) project.

First, the profiler radial velocity measurements from two storms are compared statistically to radial velocity measurements of the Wyoming Cloud Radar (WCR) aboard the NSF/NCAR C-130 using Contoured Frequency by Altitude Diagrams (CFADs). The WCR analysis shows a narrow spread in velocities with 1-2 $ms^{-1}$ wide distributions in the lower stratiform portions of the cloud, and wider distributions with 3+ $ms^{-1}$ spread in velocities in the top two km below cloud top where convective tops were observed. In the more convective region, a wider velocity distribution spanned the depth of the convective towers which were 7-8 km deep. The profiler shows similar presentation of the storms. However, the profiler did not sense the top 1-2 km of echoes that the WCR sensed, which implies the profiler lacks sufficient sensitivity to detect the cloud top convective region. This suggests that the profiler velocities are better suited to detect regions of deeper convection, rather than the cloud top convection common in the stratiform region.

The first method to extract vertical air motions from the profiler, the lower bound method, uses Doppler spectra to calculate vertical air motions. The lower bound method indicated that for the cyclone that impacted the Midwestern US on 11-12 February, 2009, the warm side of the wraparound region has the strongest vertical motions, ranging from 1-6 $ms^{-1}$, with magnitudes of 1-3 $ms^{-1}$ in the cold side of the wraparound and warm frontal shield. However, examination of another cyclone from 8-9 December, 2009 shows that the profiler has significant side lobe return, making the lower bound method unsuitable for use.

The second method first estimates reflectivity-weighted mean terminal velocities from ice particle spectra and then subtracts this mean terminal velocity from the measured radial velocity. The radial velocity is not sensitive to side lobes like the lower bound method, making this method more robust. This analysis shows a similar field of vertical motion as the lower bound method, but with slightly weaker peak vertical velocities of 4 $ms^{-1}$. The strongest vertical motions are on the warm side of the wraparound region, with the deepest updrafts extending up to 5 km in depth. The vertical motions also show that in the warm frontal region as well as the cold side of the wraparound, almost all the upward air motion is within 1 km of cloud top. The vertical motions are then related to RUC profiles of equivalent potential temperature with respect to ice over the instrument site. These profiles were created from hourly forecasts from the model run prior to the arrival of the feature of interest. The time periods of deeper convection with vertical motions greater than 2 $ms^{-1}$ corresponded to periods with potential instability.

# TABLE OF CONTENTS

## 1. Introduction

Precipitation banding is a common feature in the northwest quadrant of wintertime cyclones (Novak et al. 2004). This quadrant is typically the location of warm occluded structure and a feature known as the trough of warm air aloft, or "trowal" (Martin 1998a, Martin 1999). The feature is often referred to as the "wraparound" precipitation region. The warm occlusion process has been studied for years, starting with a model developed by Bjerknes and Solberg (1922). Our current understanding of the occlusion process is reviewed in Schultz and Vaughan (2011). The wraparound precipitation in these regions is produced by "generating cells" at cloud top, and the precipitation produces linear banded features on radar (Marshall 1953, Wexler 1955, Wexler and Atlas 1959, Carbone and Bohne 1975, Hobbs and Locatelli 1978).

The cause of these bands has been ascribed to several different mechanisms in the literature, including potential instability (Kreitzberg and Brown 1970), and more recently conditional symmetric instability, where frontogenesis forces multiple parallel bands in a slantwise unstable environment (e.g. Bennetts and Sharp 1982; Seltzer et al. 1985; Reuter and Yau 1990; Nicosia and Grumm 1999) or a single band mode in slightly stable environment (e.g. Thorpe and Emanuel 1985; Sanders and Bosart 1985; Sanders 1986).

Conditional symmetric instability in particular has been applied inconsistently when used in the literature (Schultz and Schumacher 1999). One of the difficulties in arriving at a definitive mechanism has been the relative dearth of mesoscale observations of mid-latitude cyclones. Many of the observations of cyclones come out of the CYCLES project in the Pacific Northwest (Hobbs et al. 1980; Herzegh and Hobbs 1980, 1981; Houze et al. 1981; Wang et al. 1983; Wang and Hobbs 1983; Locatelli and Hobbs 1987; Hertzman and Hobbs 1988; Hertzman et al. 1988), with other studies occurring in the

Northeastern US (e.g. Sanders and Bosart 1985; Wolfsberg et al. 1986) and in the Midwest (e.g. Carbone and Bohne 1975; Rauber et al. 1994).

One delineator between potential band formative mechanisms of the is vertical air motion. Past studies have suggested that vertical motions range from 0.6 $ms^{-1}$ as measured by vertically pointing radar (Herzegh and Hobbs ,1980), 0.2 $ms^{-1}$ at a 40 km scale (Rauber et al. ,1994), and 0.15 $ms^{-1}$ derived from two-dimensional divergence in aircraft data (Wolfsberg et al ,1986). The recently completed Profiling of Winter Storms (PLOWS) project was performed in part to provide a high resolution view of vertical motions in precipitation bands of cyclones on the scale of 1 km or less. PLOWS had multiple vertically pointing radar systems as well as sounding systems to provide a more complete view of the vertical motions in precipitation bands within continental winter cyclones.

High resolution observations of vertical motions can be compared to known properties of instabilities from the literature. While potential instability is limited solely by the environmental stability, symmetric instability has a theoretical maximum velocity under inviscid conditions of ~1 $ms^{-1}$ (Emanuel 1983; Bluestein 1993, 556–559). With friction and entrainment, this maximum is reduced to be on the order of 0.1 $ms^{-1}$, as found in numerical simulations of symmetric instability release (e.g. Bennetts and Hoskins 1979, Xu 1992, Persson and Warner 1995, Innocentini et al. 1992, Zhang and Cho 1995).

This paper will describe work performed to deduce vertical motions using a 915 MHz profiler (a part of the University of Alabama-Huntsville Mobile Integrated Profiling System, or MIPS) in fine scale bands within continental winter cyclones observed during PLOWS. Section 2 describes a statistical comparison of radial velocities from the profiler and another radar (the Wyoming Cloud Radar, WCR, aboard the NSF/NCAR C-130) in order to better understand how the profiler senses the storms, and to provide context for interpreting data from the profiler. Section 3 presents an analysis of vertical motions

derived from wind profiler data using the methodology from Cronce et al. (2007); in this analysis, a problem in utilizing the methodology with wind profilers is identified. Section 4 describes an alternative methodology for deriving the vertical motions from wind profiler radial velocities. Section 5 will summarize the findings of this work.

## 2. Comparisons of Profiler and Cloud Radar Radial Velocities

### *2.1 Methodology*

In this section, the radial velocities measured by the MIPS and WCR are compared. The MIPS profiler is a 915 MHz profiler with a 9 degree beamwidth, 106 m vertical resolution, and 40 sec between beams. The WCR is a W-band (94.92 GHz) radar with a beamwidth of 1 degree and 15 m vertical resolution, with 0.5 sec between beams.

In addition to the difference in design, a different sampling strategy was employed for the two systems. The wind profiler was positioned in one place prior to the arrival of a storm and the storm moved overhead in time. Storms took up to a day to pass over the profiler, during which time they evolved. The WCR, mounted on the C-130, moved through the storm as time progressed. Most flight legs took an hour or less to complete so that the storm during a WCR cross-section evolves much less than during a profiler time-section. Because the C-130 flight legs were not directly over the MIPS for most of PLOWS, the C-130 did not typically sample the same features sampled by the wind profiler, presenting a challenge in comparing the two datasets.

To do the comparison, important features observed by both the MIPS and WCR were identified. Further, the time difference between the profiler and WCR's measurement of a feature was kept to a minimum. Then, storm features common to both datasets with similar radar presentation on both the MIPS and WCR were selected for comparison. These cyclone features were also located in the same spatial region of the storm, such as the edge of the wraparound region, to ensure that the compared features were as similar as possible.

For the features identified for comparison, the radial velocity measurements from the MIPS and WCR were used to create Contoured Frequency by Altitude Diagrams (CFAD, from Yuter and Houze 1995). The WCR data was resampled to a height resolution of 106 m AGL, the size of the profiler range

gates, in order to construct these diagrams. All radial velocities in each altitude bin were divided into 0.2 $ms^{-1}$ velocity bins and normalized to the number of vertical profiles in that altitude bin. This creates a CFAD with identical bin sizes in altitude and velocity for the WCR and profiler to reduce the effects of the different sampling volumes. The normalization also accounts for the differing number of samples between the two radars.

These CFADs were then compared for corresponding features of the storm. While the observations were matched as close as possible to represent the same areas of the sampled storm, an exact space and time comparison is not possible. Instead of looking for an exact correlation, the CFADs are compared to see what general features are detected by both systems, as well as to contrast the general appearances to ascertain how the platforms view the cyclone's features.

### *2.2 Results*

Three separate comparisons using CFADs, two from PLOWS IOP 10 (8-9 December, 2009), and one from IOP 9 (2-3 December, 2009) are shown below. Figure 2.1 shows the WSR-88D radar composite valid at 0300 UTC on 9 December overlain with the C-130 flight track for the flight leg used in this analysis. For reference, the MIPS profiler location is also shown.

The reflectivity from the WCR along this flight leg is shown in Figure 2.2a alongside the radial velocities in Figure 2.2b. For this flight leg, the warm (south) side of the wraparound is on the right. Figure 2.3 a and b show the signal to noise ratio (SNR) and radial velocities recorded by the MIPS profiler for IOP 10. Each figure has a box over the regions compared with CFADs.

The boxes labeled with "W" indicate the data used to create the CFADs for the warm side of the wraparound for each radar system, and the boxes labeled with "C" indicate the data used to create the CFADs for the cold side of the wraparound. The WCR CFAD for the warm side is presented in Figure 2.4a.

Positive velocities are defined as upward. Each box is colored according to the number of observations in each velocity bin, normalized by the number of vertical profiles in the dataset. For reference, the number of observations in each altitude bin is plotted next to the CFAD. The sum of values at an altitude will not necessarily be 1 because the denominator used for normalization includes profiles where there was noise at each altitude. The sum of all values in displayed bins in a CFAD and the percentage of noise samples bins with noise (not shown) would equal 1 for every altitude. Bins were only plotted if they contained at least 200 noise-filtered velocity values to ensure a small number of observations did not produce an unrepresentative distribution.

The WCR profile shows a narrow distribution of velocities near the ground, with a widening distribution with altitude. The distribution expands with altitude to reach a peak upward velocity of 5 $ms^{-1}$ around 5 km, and displays values greater than 1 $ms^{-1}$ for most elevation gates above 3 km. Significant downdrafts are also seen with values to -3 $ms^{-1}$ present throughout the profile. The data tops out at about 8 km, an altitude near the tropopause.

Figure 2.4b shows the same analysis performed for the MIPS profiler in the warm part of the wraparound, as indicated by the box in Figure 2.3. The MIPS CFAD has the same general characteristics of the WCR CFAD. The distribution is fairly narrow near ground level, and spreads out significantly above 3 km. The distribution widens to +5 $ms^{-1}$ on the positive side and to -5 $ms^{-1}$ on the negative side. The area of detectable velocities is shallower, with the top of the distribution at about 7 km. The modal values, the shape of the distributions as a function of height, and the overall characteristics are remarkably similar to the WCR, except that the profiler cannot detect the smallest particles at the top of the storm above 7 km altitude.

This analysis was also performed for the cold side of the wraparound for both systems. Figure 2.5a shows this analysis for the WCR in the cold side of the storm from the “C” box in Figure 2.2. The cold side of the wraparound region is characterized by a much deeper region with a narrow velocity

distribution as a function of height. The velocity distribution spreads only within the upper 2-3 km of echo where the velocities range to ±3 $ms^{-1}$. The area near cloud top is where the WCR reflectivity shows cloud top convective structures in the cross sections. The top of the distribution was about 9.5 km, at the tropopause.

The MIPS CFAD for the cold side of the wraparound region is shown by Figure 2.5b. Again, the moral values, the shape of the distributions as a function of height, and overall characteristics are remarkably similar, except that the profiler cannot detect the smallest particles at the top of the storm above 7 km altitude. The overall presentation of the cold side wraparound is similar with a deep region with little velocity variation. There is a spread in velocities near 7 km, but the larger spread is only evident on the WCR. Peak velocities observed by the profiler are less than 1 $ms^{-1}$, with downward velocities on the other side of the distribution of less than 2 $ms^{-1}$.

Another comparison of the two radar velocity distributions was performed using data from PLOWS IOP 9. The WSR-88D reflectivity composite with C-130 flight track and MIPS location is shown as Figure 2.6. The WCR and MIPS data from this system are shown in Figures 2.7 and 2.8, respectively. Only the convective region, the warm side of the wraparound, was used for comparison, as this was the only area common to both datasets. These features are outlined by the boxes, and are located on the warm side of the wraparound.

The CFAD generated from the WCR data is shown in Figure 2.9a. While this part of the profile is on the warm side of the wraparound, it resembles the cold side profiles from IOP 10 in that the distribution of velocities is fairly narrow with height for much of the profile. As this is a rain event at the surface, the melting level is evident in the velocity regime shift at approximately 1 km. The exception to the narrow distribution is once again near echo top, where velocities spread out to ±2 $ms^{-1}$, again where the reflectivity shows the convective echoes. Echo top for this region is at approximately 9.5 km.

The MIPS profiler CFAD is shown as Figure 2.9b. The profile shows good agreement in the distributions at altitudes where data exists for both systems. Again, the MIPS did not detect particles at the higher altitudes, with the top of the profile located at 6.5 km. The edges of the distribution widened again at echo top, reaching from -3 $ms^{-1}$ to +1 $ms^{-1}$.

*2.3 Discussion*

When comparing the CFADs, the overall agreement in the velocity distributions stands out. Despite the fact that the radars do not have the same characteristics or sampling strategies, and despite the fact that the storm evolved in time between the time that the radars observed it, the vertical distribution of radial velocities was remarkably similar for comparable regions of the storm. Common elements, such as the bright band in IOP 9, show up as not only at the same location, but also with velocities of similar magnitudes. This gives us confidence that both systems are sampling similar structures, and that the comparisons made with the CFADs are robust.

Near the top of every profile with the WCR, the distribution broadens. This is a manifestation of the cloud top instabilities noted in the WCR by the small-scale convective reflectivity fingers at the top of the storm. While the upward motions are not always of a large magnitude, this feature is seen in all of the CFADs.

The CFADs from the warm side of the wraparound of IOP 10 both showed a large range of vertical velocities, in both the upward and downward directions. This is a signal of deep vertical convection, and the deep convective profile was present in both datasets with similar magnitudes. This deep convection manifests itself in the CFAD by the large upward and downward motions of greater than 2 $ms^{-1}$ that extend for several km deep. The cold side of the wraparound CFADs from each radar IOP 10 also matched well with each other, but the matching structures here were limited to the narrow

velocity distributions through much of the profile, while the cloud top instability illustrated by the broadening of the velocity distribution near cloud top, was only detected by the WCR. For the IOP 9 case, a similar pattern was noted, namely the deep, narrow distribution agreed, but the widening near cloud top was detected only by the WCR.

Given the similarity of the CFADs from independent measurements from the WCR and MIPS, there is confidence that the velocity profiles are reasonable. However, the CFADs are not identical. The WCR CFADs extend deeper vertically than the MIPS profiler CFAD. While it is possible that system evolution caused this, the fact that it occurs for all of the cases examined suggests that the profiler is not sensitive enough to detect cloud tops. The WCR shows that this is where the convective structures are located on the cold side of the wraparound, so we can expect that the profiler will not provide returns to the top of deeper systems, and will not detect this important part of the storm. Thus, the best use of the MIPS profiler in PLOWS is to investigate the deeper convective structures more likely to occur on the warm (dry slot) side of the wrap-around band.

*Chapter 2 Figures*

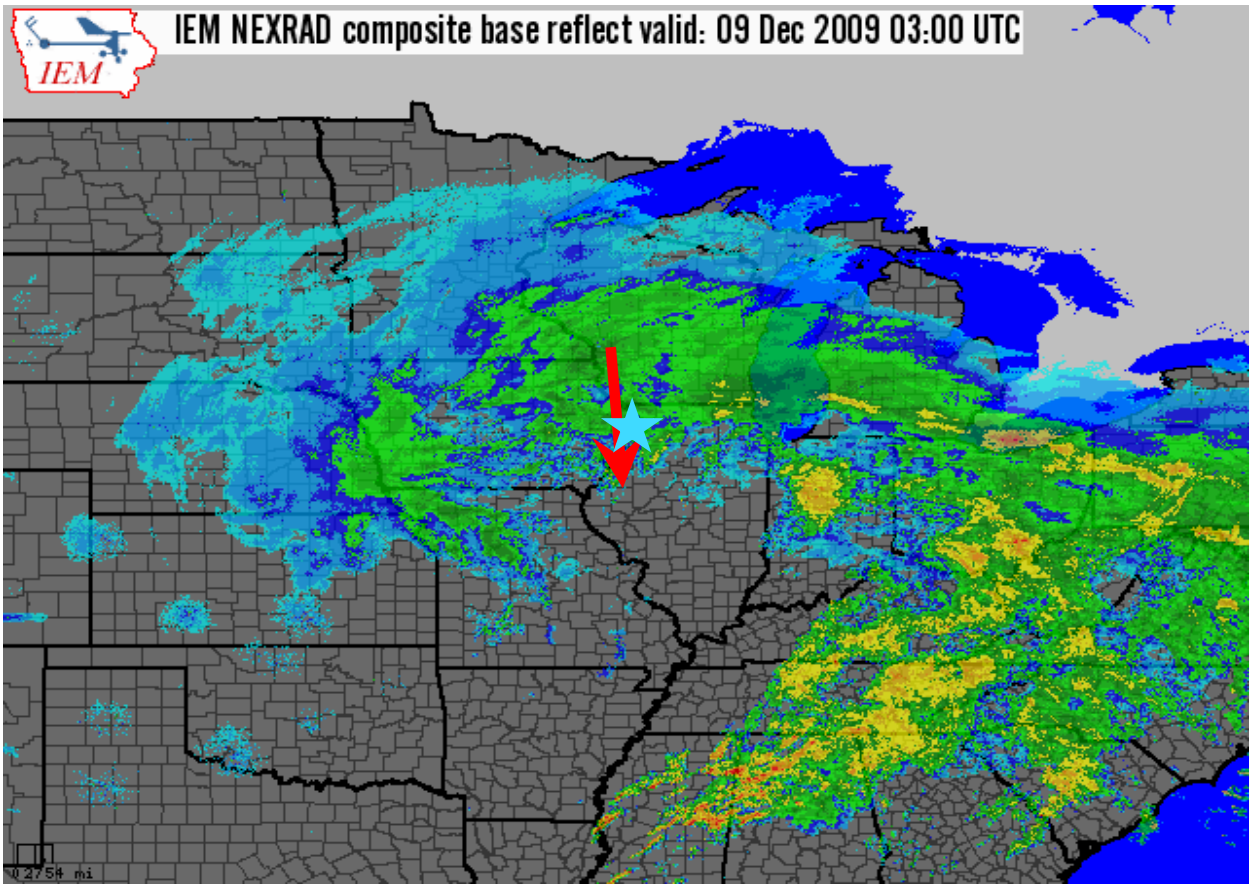


Figure 2.1: WSR-88D radar composite for IOP 10 valid at 0300 UTC on 09 December, 2009. The arrow indicates the C-130 flight path and direction for the flight leg used in this section. The star indicates the location of the MIPS profiler.

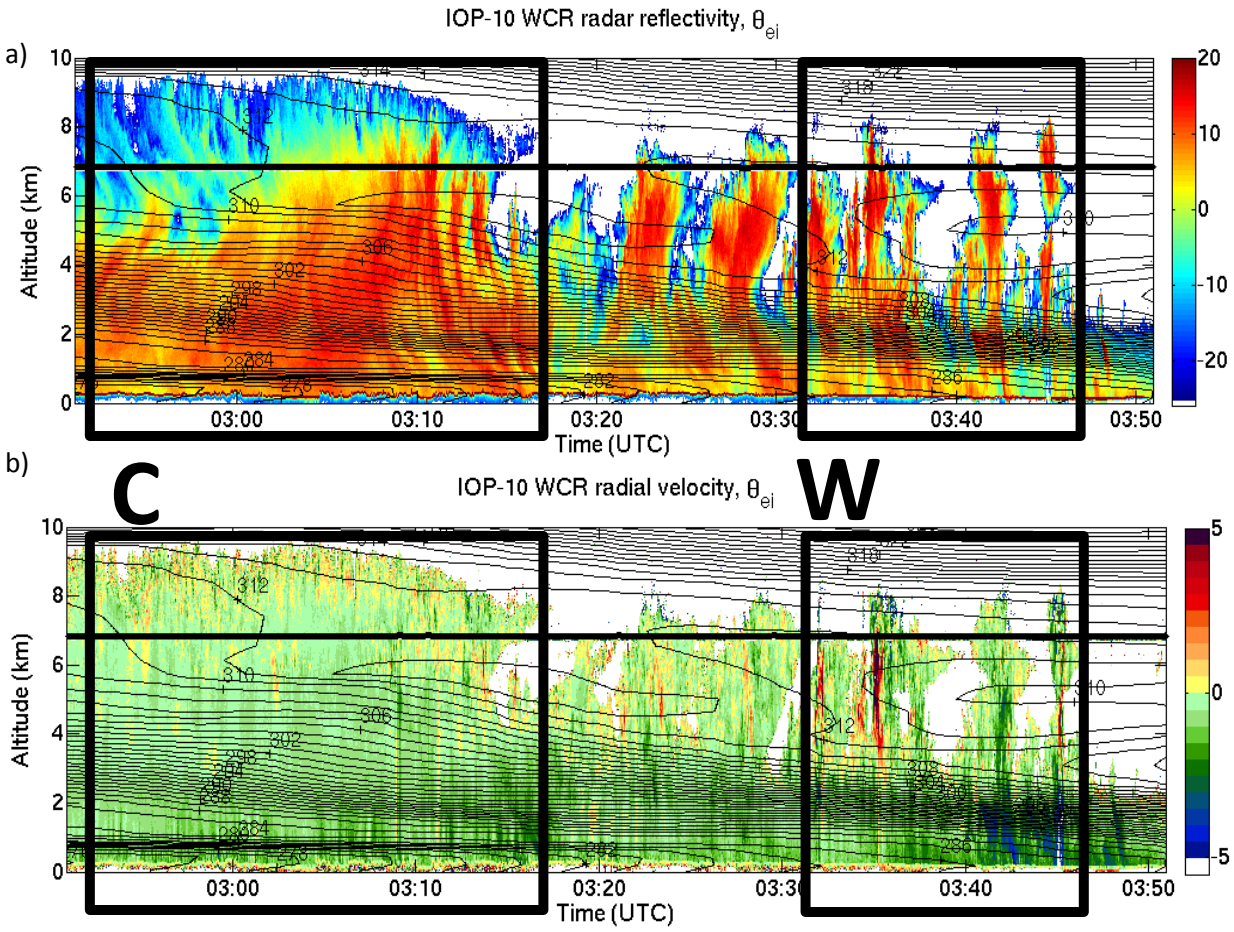


Figure 2.2: WCR a) reflectivity and b) radial velocity values overlain with RUC equivalent potential temperature with respect to ice values for the flight leg indicated in Figure R3.1. The boxes indicate regions where CFAD analysis was performed.

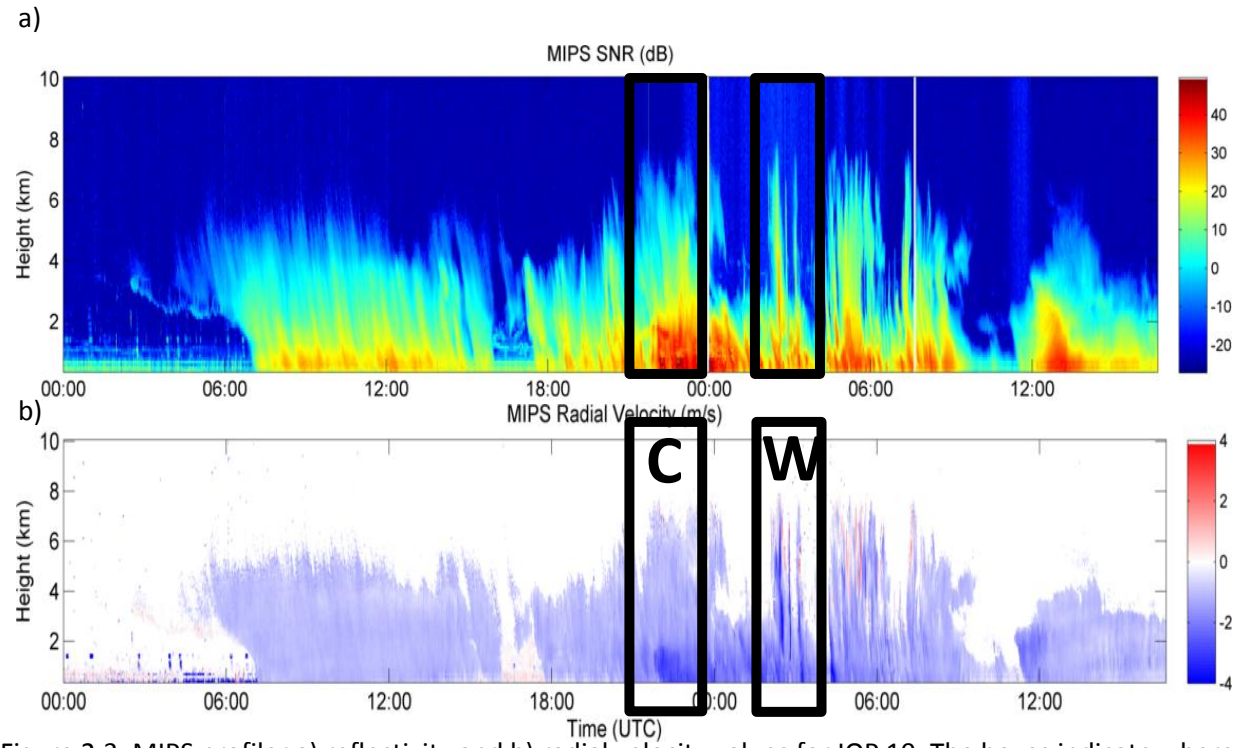


Figure 2.3: MIPS profiler a) reflectivity and b) radial velocity values for IOP 10. The boxes indicate where the CFAD analysis was performed.

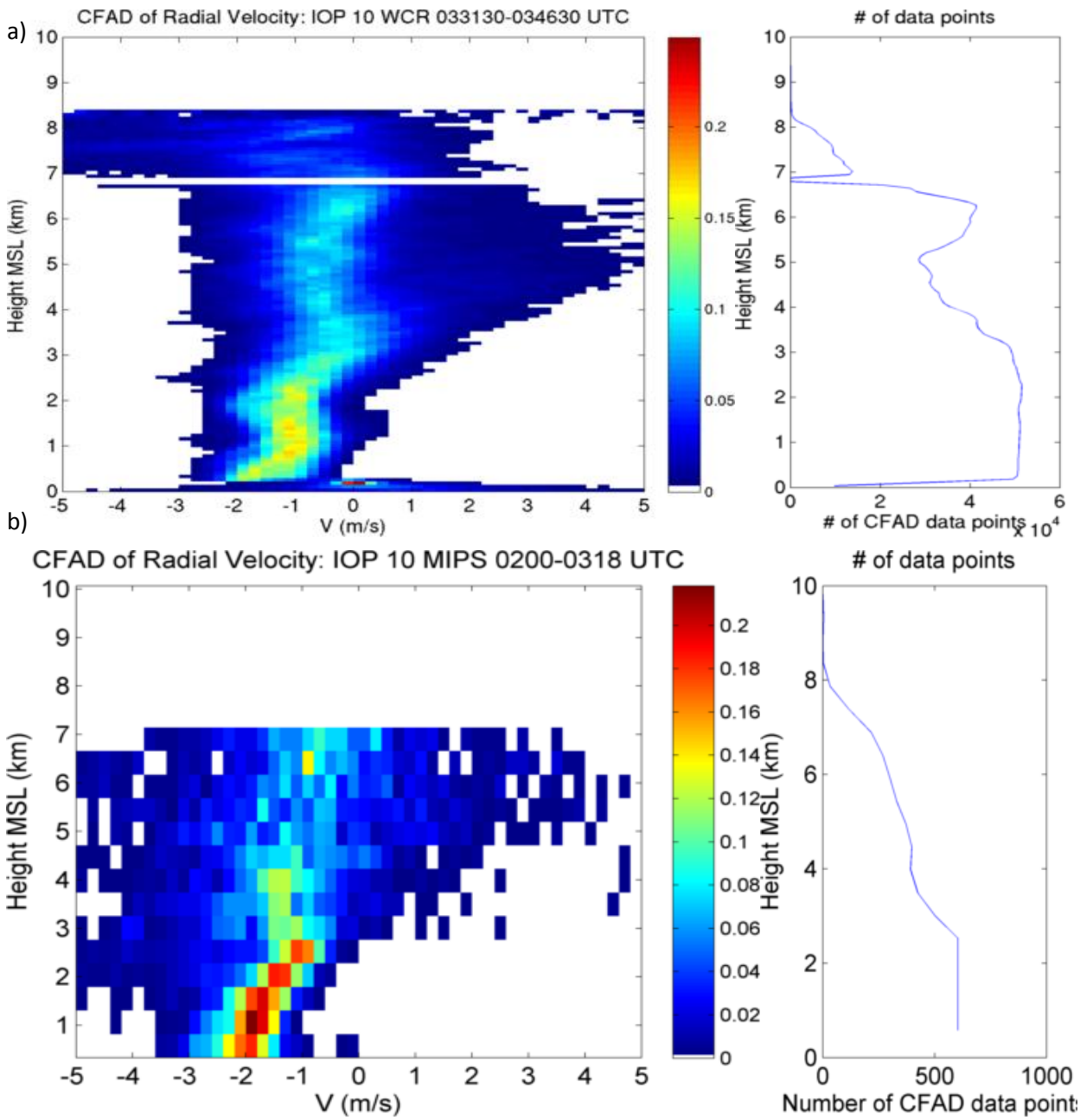


Figure 2.4: CFAD diagrams for the a) WCR and b) MIPS for the "W" boxes in Figure 2.2. Data is normalized to number of vertical profiles in the dataset, shown as a function of altitude on the right.

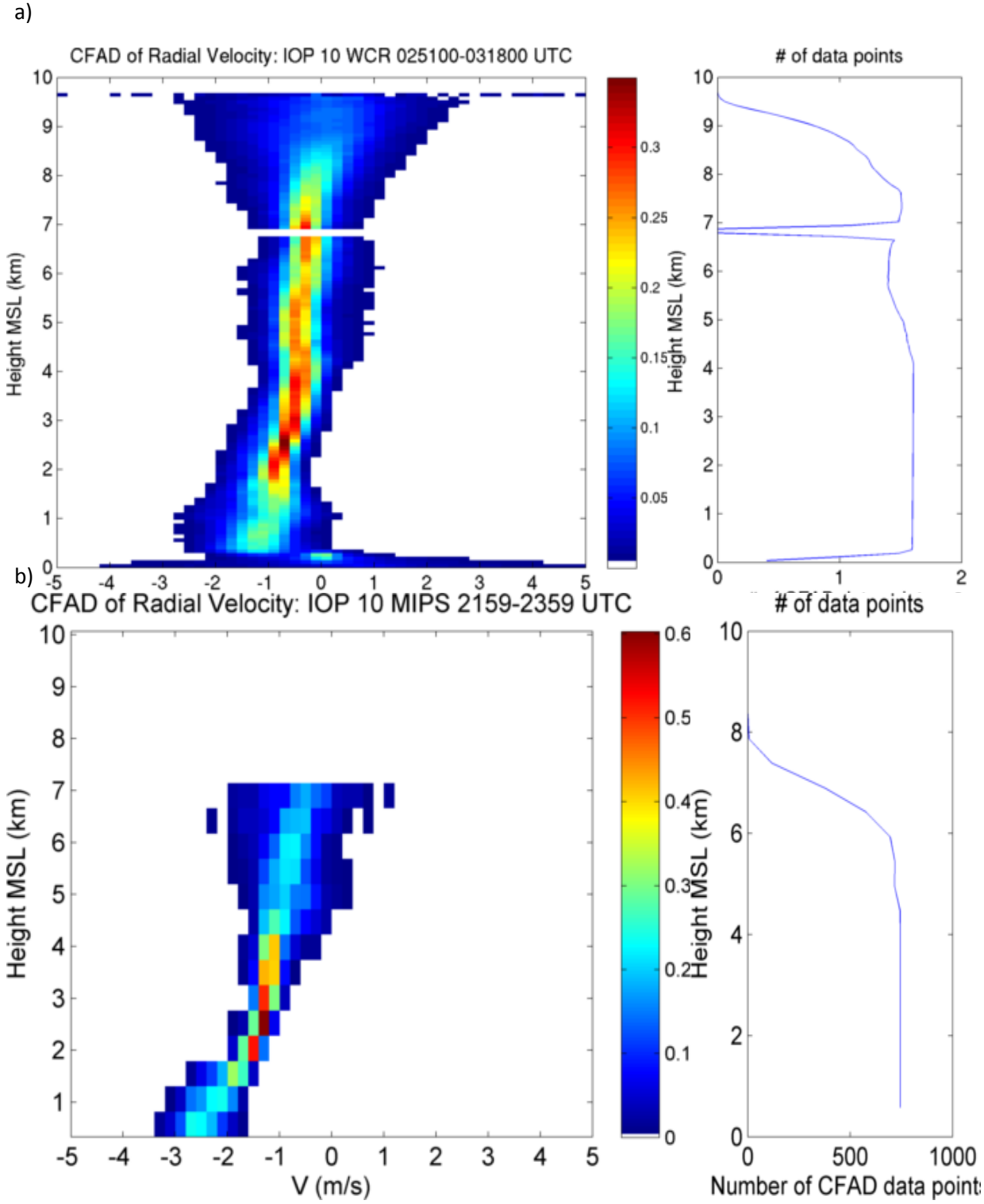


Figure 2.5: Same as Figure 2.4, but for the "C" regions.

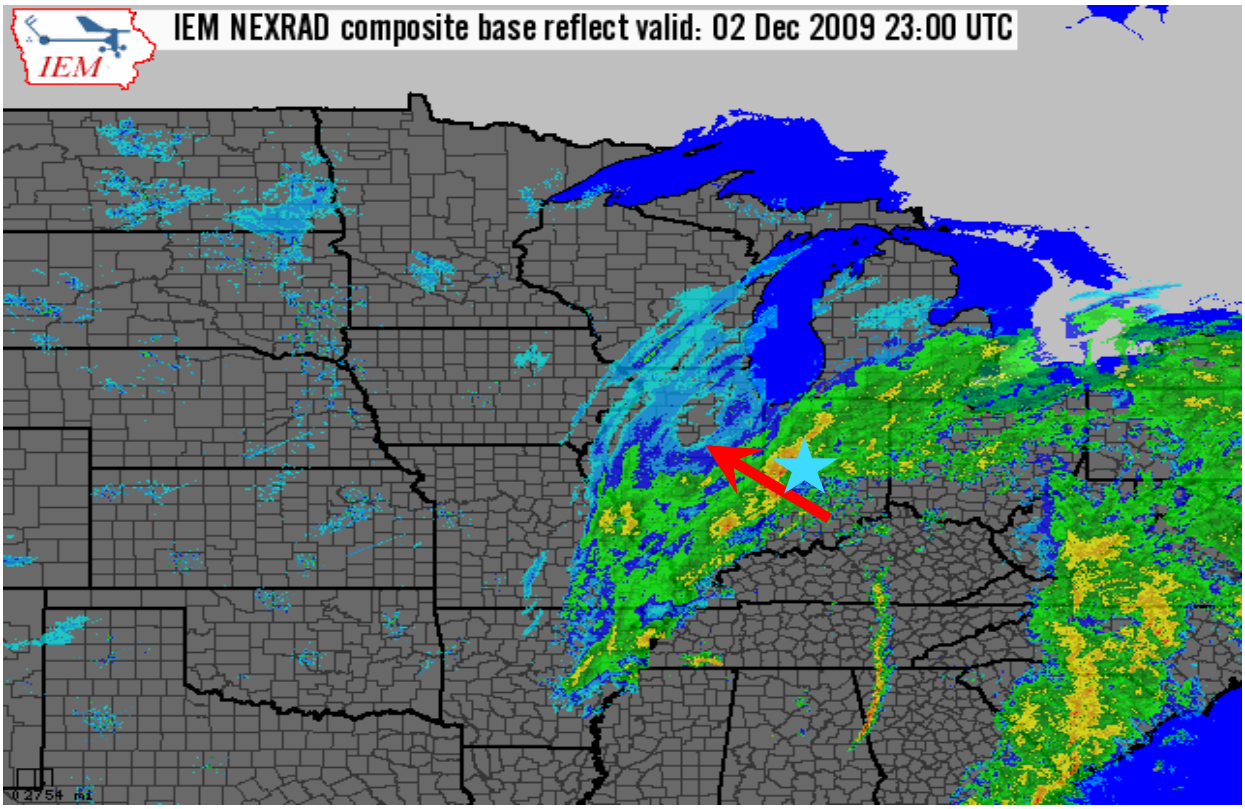

Figure 2.6: Same as Figure 2.1, except for IOP 9. Radar image valid 02 December 2009 at 2300 UTC.

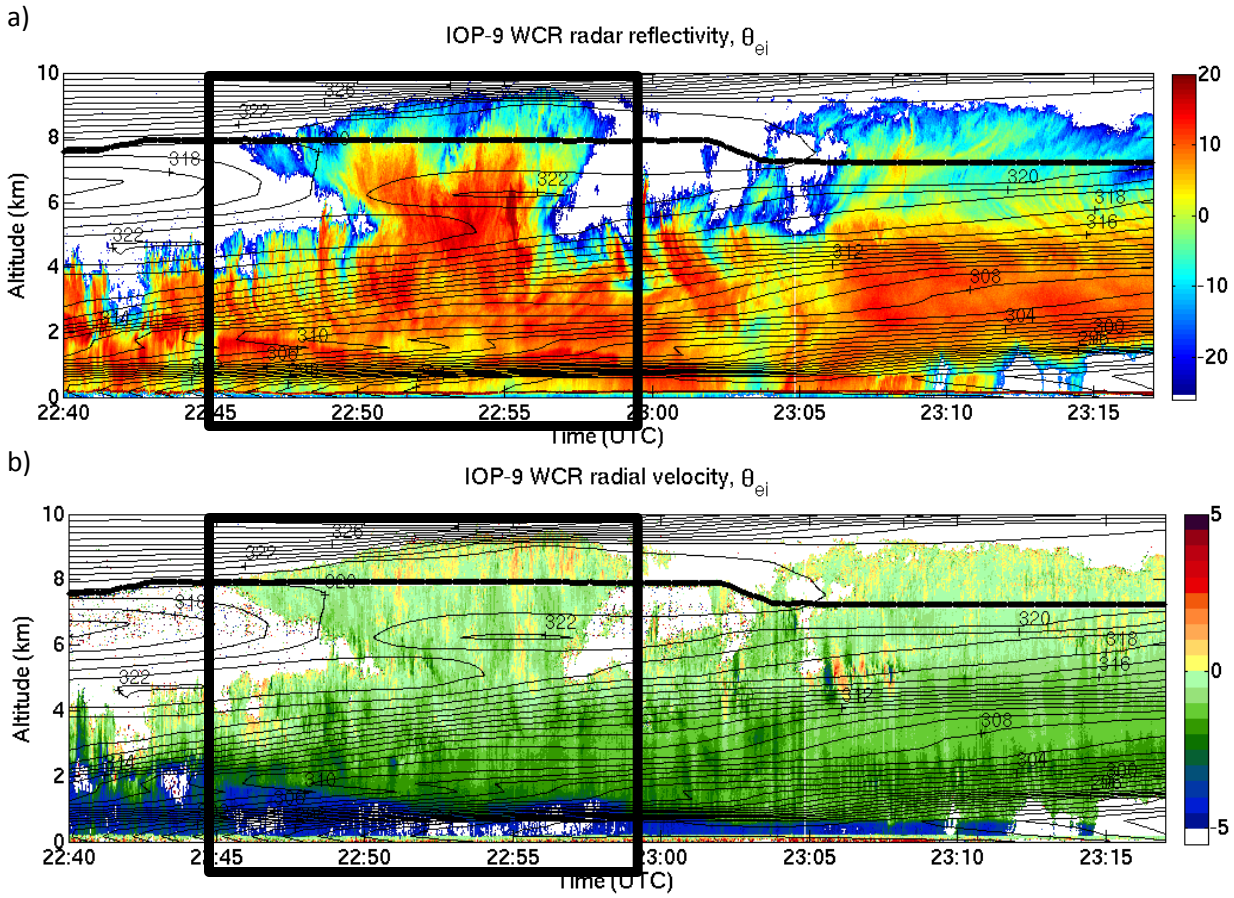


Figure 2.7: As with Figure 2.2, but for the flight leg in Figure 2.6. The box indicates the location for the CFAD from IOP 9.

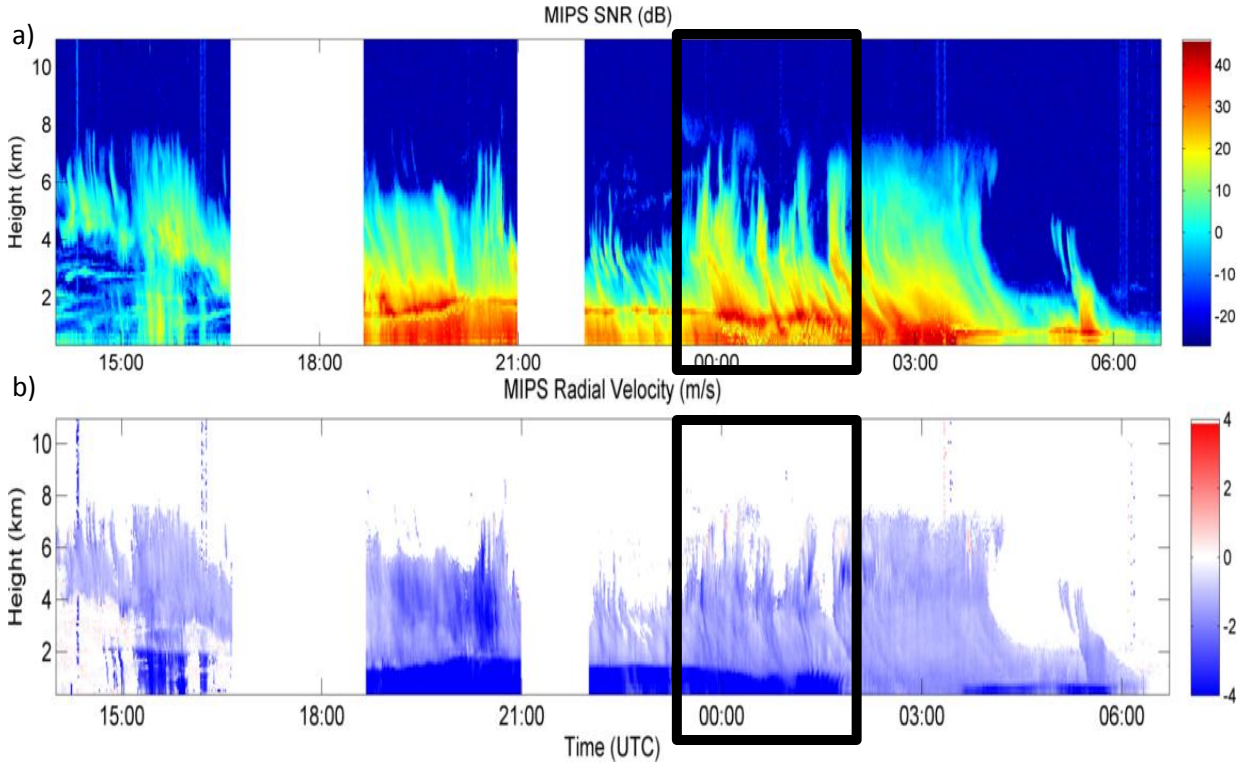


Figure 2.8: As with Figure 2.3, but for IOP 9. The box indicates the location of the CFAD from IOP 9.

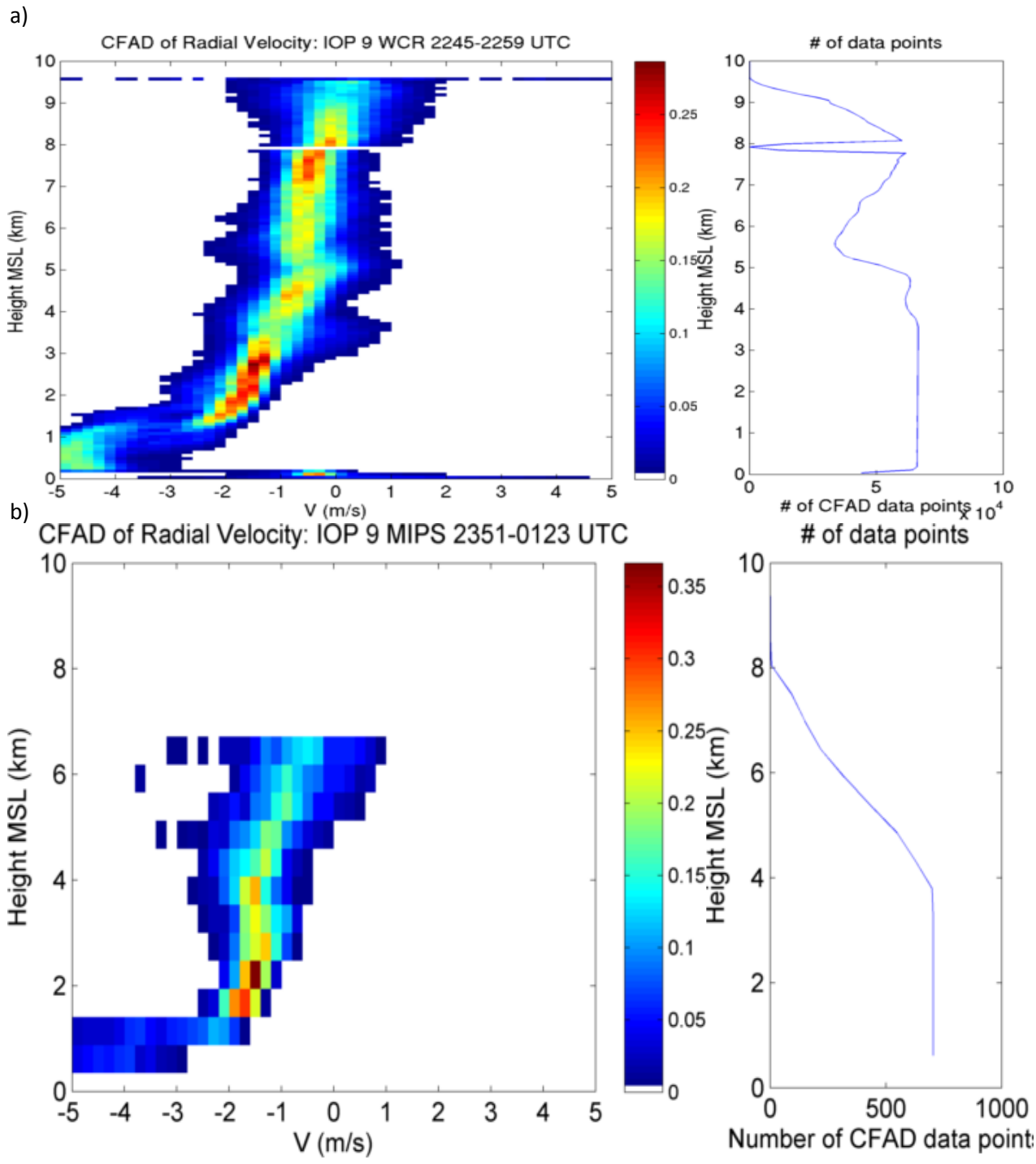


Figure 2.9: As with Figure 2.4, but for the IOP 9 region.

## 3. The 11-12 February 2009 Cyclone

The 11-12 February, 2009 cyclone was used to develop the analysis tools to perform the lower bound method calculations. Figure 3.1 (a) shows the 500 hPa analysis valid at 0000 UTC on 11 February. There was a shortwave over the upper Midwest from a previous cyclone. At this time, the IOP 1 shortwave is located over New Mexico. Fig. 3.1(b) shows a cyclone near the Ontario-Minnesota border with a quasi-stationary front extending from it across the central United States west to the IOP 1 cyclone, which was located in extreme southeastern Colorado. Over the next day, the IOP 1 shortwave moved into the Midwest, so that its axis was over Indiana at 00 UTC on 12 February, as shown in Fig. 3.1(c). The associated surface cyclone propagated along the quasi-stationary front with the shortwave, with the cyclone centered over southwestern Michigan at 0000 UTC on 12 February, as indicated in Fig 3.1(d).

For this storm, the MIPS 915 MHz wind profiler was deployed south of Chicago, IL, with the profiler location indicated by the star in Figure 3.2. The profiler was operated continuously as the storm passed overhead from 0718 UTC 11 February to 0004 UTC 12 February 2009. The profiler recorded signal-to-noise ratio, radial velocity, spectral width as well as Doppler spectra with 40 second temporal and 108 m vertical resolution. In addition, wind profiles were calculated and averaged over 30 minutes to reduce noise. Since the MIPS profiler operates at a frequency of 915 MHz, it does not detect Bragg scattering when Rayleigh scattering is occurring due to precipitation (for a detailed explanation, see Cronce et al. 2007, Appendix A).

In addition to the profiler measurements, soundings were launched by the University of Missouri on the northwest of the profiler site at the location indicated on Figure 3.2. The sounding system was approximately 25 km away from the profiler. The sounding system was only set up at 1200 UTC on 11 February, and soundings were launched approximately every three hours thereafter. Three

soundings failed at approximately 700 hPa as the balloons broke when they froze. A second sounding was launched after each initial attempt that failed, but there was a significant gap in the sounding data around 2100 UTC as both the original and replacement soundings failed.

Figure 3.3 shows two WSR-88D composite images with the profiler location indicated by the star. The composites show the major structural features of the system, including the warm frontal precipitation, the dry slot, and the precipitation in the wraparound region. All three precipitation regions passed over the ground site, making this data set ideal for investigating the vertical structure of the storm. As the regions of precipitation passed over the profiler, several precipitation bands were sampled, especially in the wraparound region, allowing for the possibility of deriving a high-resolution picture of the vertical air motions in the system. In addition, soundings were launched through all of the major structural features of the cyclone, which provided a concurrent set of wind profiles to the profiler in addition to the thermodynamic analyses the soundings produce.

As the IOP 1 storm moved overhead, the profiler recorded a time-height path through the storm. Figure 3.4 shows the SNR values recorded by the profiler as the system passed over. The three main structural features of the storm are apparent: the warm frontal shield passed over first, as shown in 3.4a); next the dry slot moved over, indicated by the relatively weak and shallow echoes; and finally the wraparound region moved over the profiler, as shown in Figure 3.4b).

The warm frontal region, passing over from ~0900 to ~1300 UTC, was relatively uniform with echo tops generally in the 7-8 km range and the bright band rising with time as warmer air moved in. As the main area of precipitation associated with the warm frontal region moved out, the dry slot moved overhead. The near-ground echoes indicated shallow areas of precipitation that intermittently moved over the profiler, but any precipitation was light. That changed when the wraparound region moved overhead around 2000 UTC, as deep, heavy precipitation moved in again. Echoes reached 5-6 km

initially, then reached over 8 km tall on the cold side of the wraparound region. The bright band descended as cold advection set in at the surface, but never disappeared as precipitation remained in the form of rain at the surface for the duration of the storm. Based on the comparison between the WCR and the profiler in Chapter 2, the true cloud tops in this system were likely 1-2 km deeper than indicated by the profiler.

The radial velocity measurements recorded by the profiler for the IOP 1 case are shown in Figure 3.5. In the warm frontal region shown in part a), radial velocities were relatively uniform above the bright band. The only large upward velocities were associated with a mesoscale gravity wave shortly before 0900 UTC; an examination of that wave is beyond the scope of this thesis. Other than some slightly positive values at approximately 1030 UTC, no areas of significant upward particle motions were found in the warm frontal region.

The wraparound region, however, has a large area of upward particle motions. These areas began after 2100 UTC and included regions of total upward radial velocities of more than 2 $ms^{-1}$. The strongest upward motions were located close to the edge of the dry slot and extended vertically from 1 km above the bright band to near cloud top. Outside of these positive values, the rest of the wraparound region generally consisted of radial velocity values near zero, with some larger downward velocities after 2200 UTC.

*Chapter 3 Figures*

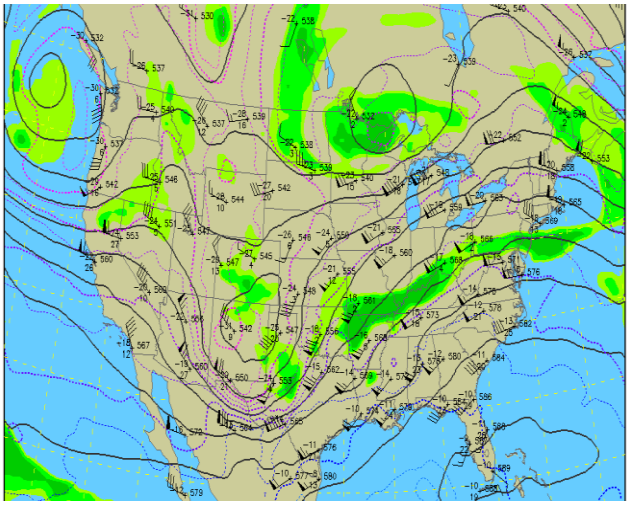

(a)

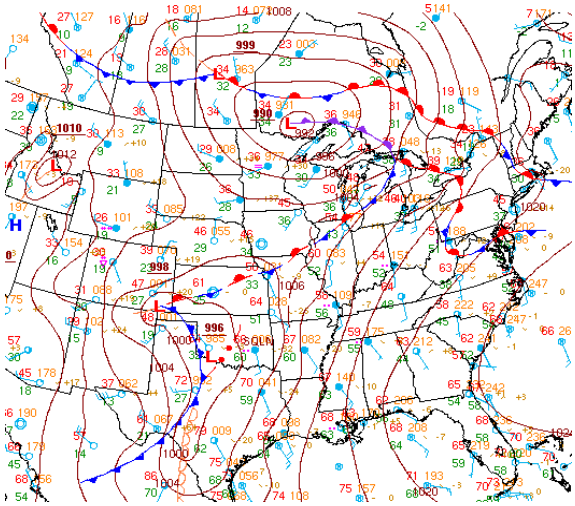

(b)

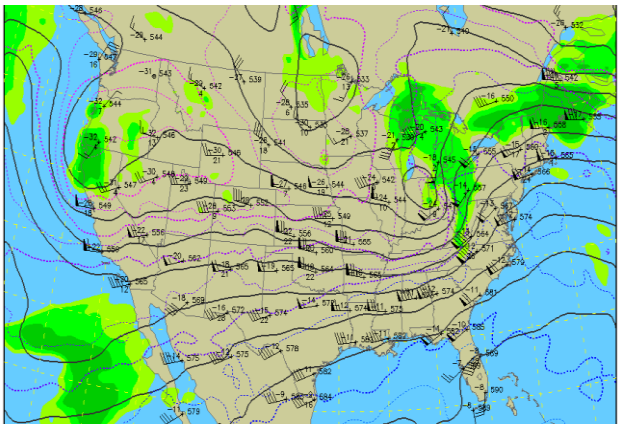

(c)

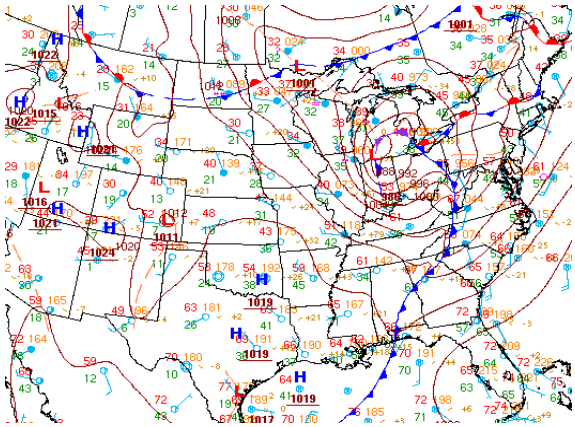

(d)

Figure 3.1: (a) 500 hPa analysis valid at 0000 UTC 11 February, 2009. Wind barbs are knots, contours are heights in km, and shading is % RH. (b) HPC surface analysis valid at 0000 UTC 11 February, 2009. Contours are pressure every 4 hPa. (c) Same as (a), but for 0000 UTC 12 February 2009. (d) Same as (b), but for 0000 UTC 12 February 2009.

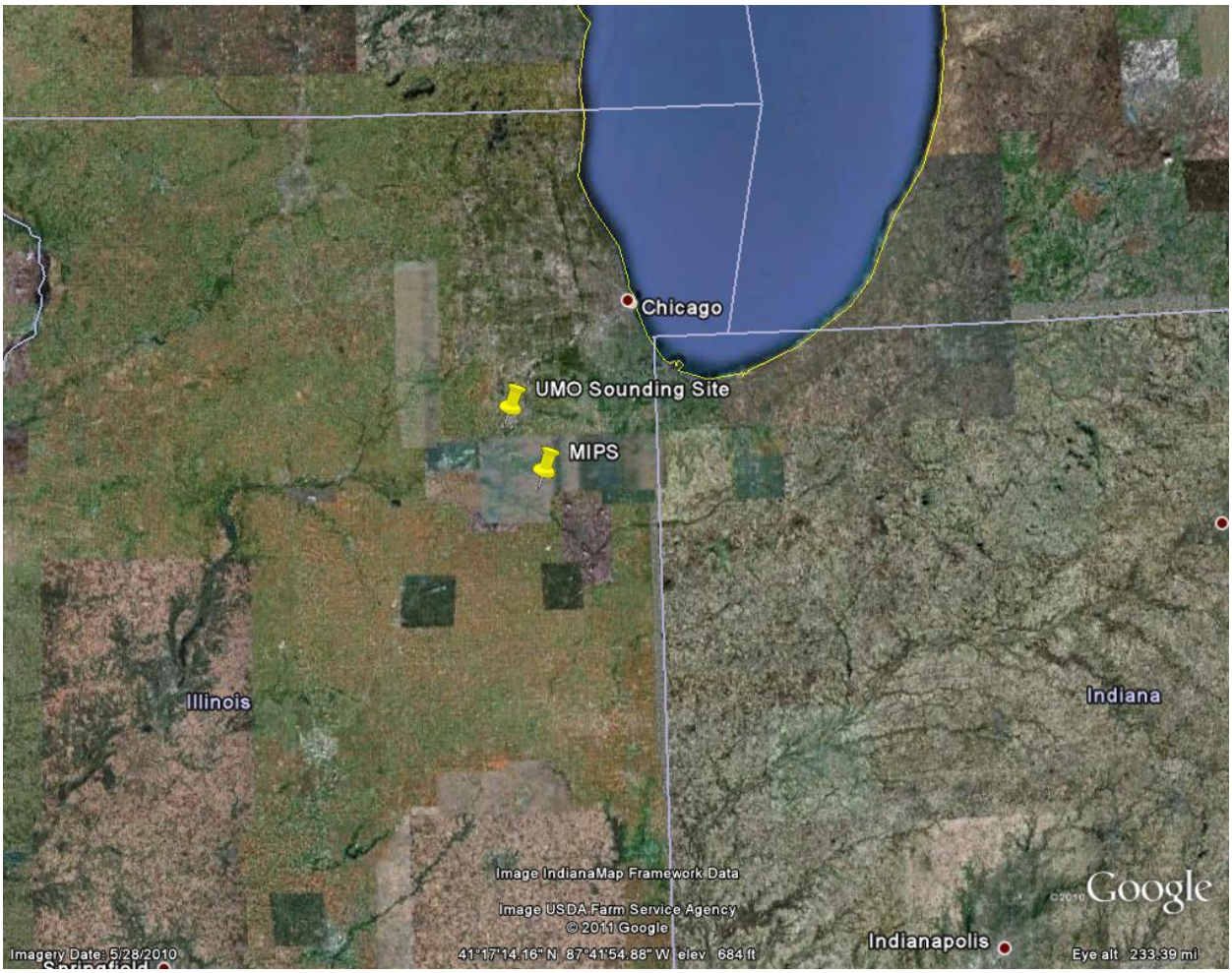


Figure 3.2: Google Earth image showing the location of the MIPS profiler and the University of Missouri sounding site.

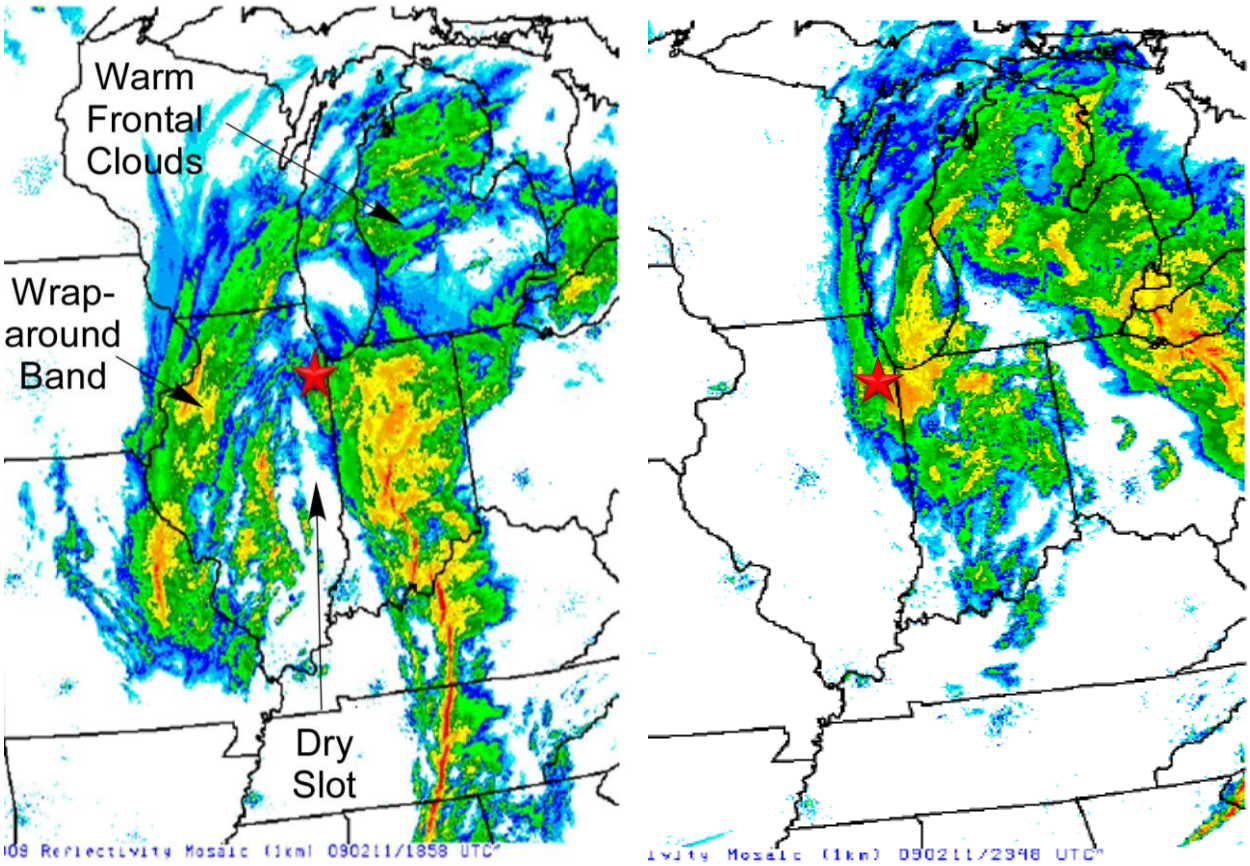


(a) (b)

Figure 3.3: (a) WSR-88D radar composite at 1858 UTC 11 February. The red star indicates the location of the MIPS profiler. At this time, the dry slot is moving over the profiler with the wraparound precipitation to the west, after the warm frontal precipitation passed overhead. (b) Same as (a), but for 0000 UTC 12 February when the wraparound precipitation was exiting the profiler location.

a)

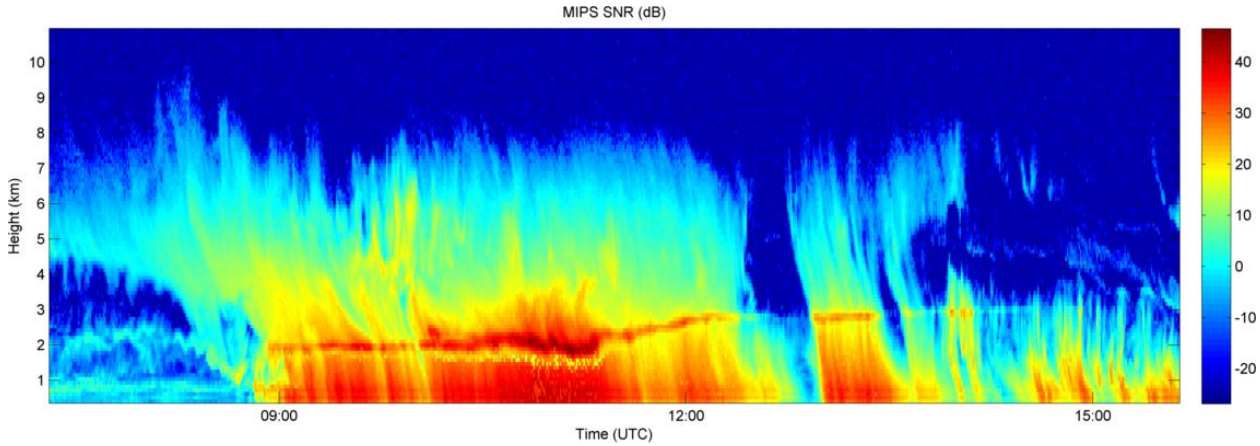


b)

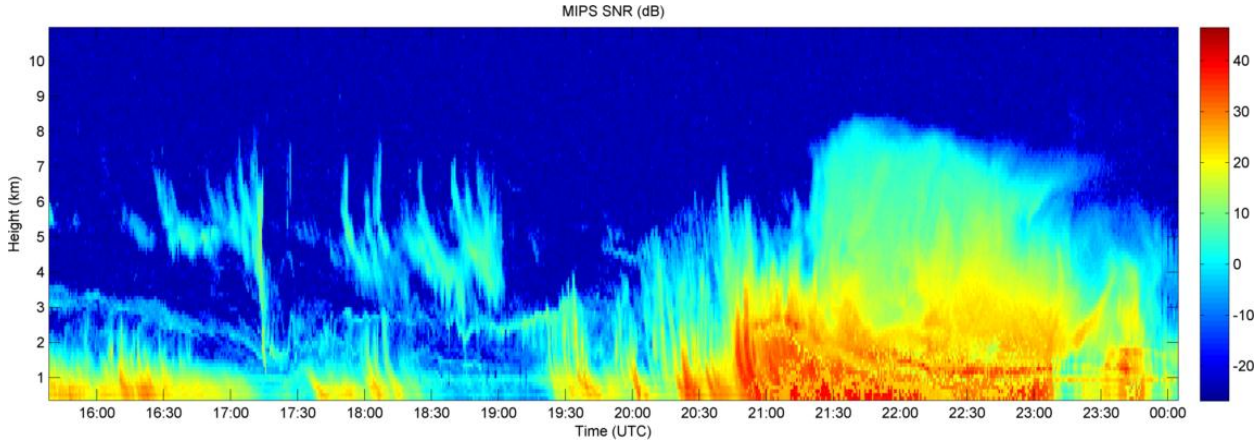


Figure 3.4: MIPS Signal to Noise Ratio (SNR) from IOP 1 in dB. Panel a) shows the warm frontal region, and panel b) shows the wraparound region. The dry slot lies in both figures between the two large areas of precipitation.

a)

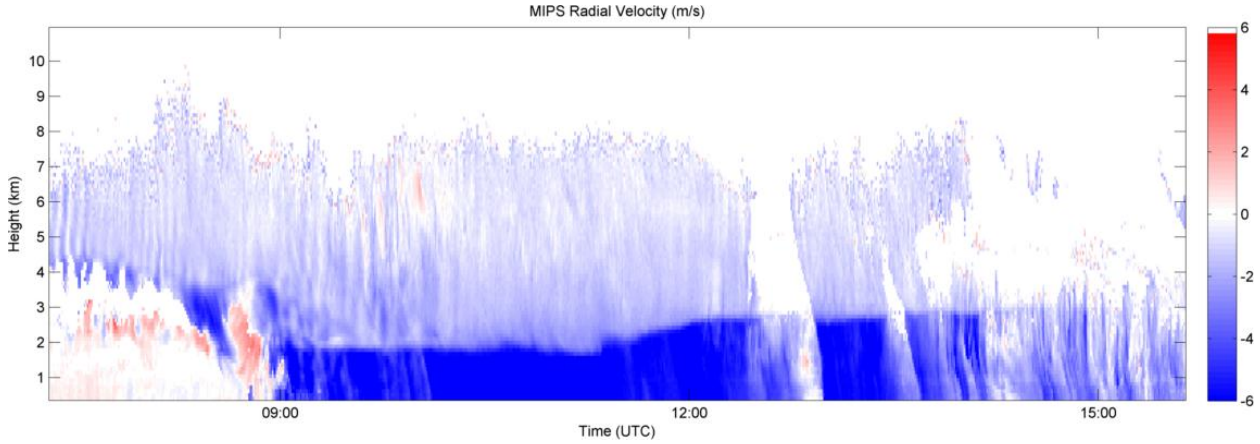


b)

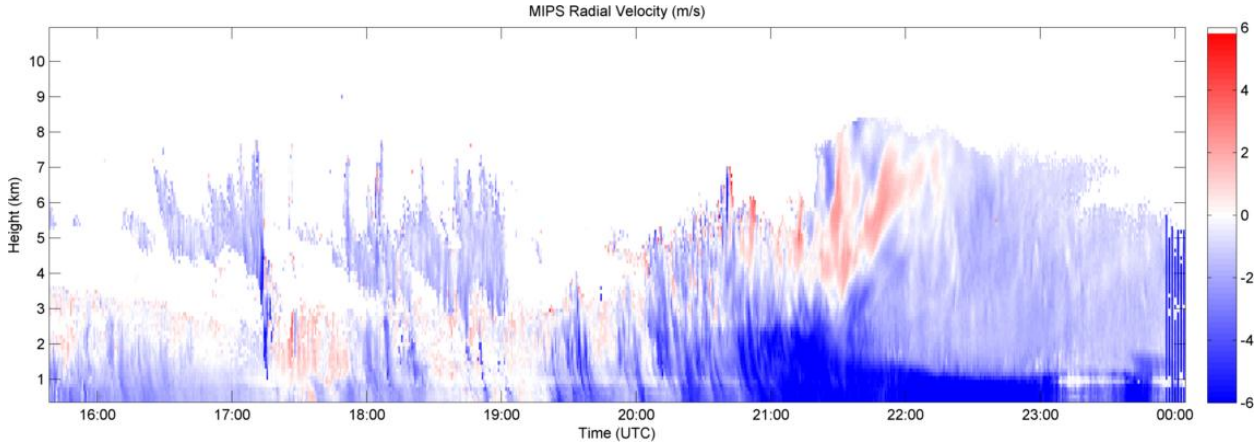


Figure 3.5: MIPS radial velocity from IOP 1 in $ms^{-1}$. a) and b) correspond to the same time periods as Figure 3.4. Positive (upward) velocities are red.

## 4. Lower Bound Method

### *4.1 Methodology*

In this section, the first method attempted for deriving the vertical air motion (*w*) from the Doppler spectrum recorded by the MIPS wind profiler is described. The lower bound method (LBM, Probert-Jones and Harper 1961, Atlas 1964, p. 413) retrieves vertical motions by first finding the radial velocity of the smallest particles detected by the radar. The LBM is described extensively in Cronce et al. (2007); this section will therefore describe only the process used to carry out the lower bound method using data acquired during PLOWS. This research here will show, however, that the LBM fails due to power leakage from sidelobe into the profiler's main beam return.

The velocity of the smallest particles can be estimated using the profiler Doppler spectrum, an example of which can be found in Figure 4.1. The power returned in each velocity bin is plotted on the vertical axis in dB, with positive velocities defined as upward, away from the radar. The solid line is the noise floor, which is calculated by averaging the power in the first sixteen and last sixteen spectral bins together. The velocity values of the sixteen bins on each end of the spectrum are well beyond the expected magnitude of particle vertical radial velocities, especially for snow, and are assumed here to contain noise. The smallest particles in the spectrum are located on the right (more positive) side of the power peak just above the noise floor, because the smallest particles have the lowest terminal velocities and hence the most positive speeds away from the profiling radar occurring in the spectra. The smallest particles' power return is defined as the power in the first spectral bin on the right side of the power peak with a power return greater than three times the standard deviation of the noise floor. The level of three standard deviations was chosen to err on the side of producing a final estimate of vertical air motion value that is conservative. The small particle total modal fall velocity is assumed to be the Doppler velocity associated with that particular spectral bin. In Figure 4.1, this power return from the smallest particles is indicated by the circle on the Doppler spectrum.

In order to find the vertical air motion, the other components of the particle motion detected by the profiler must be known and removed. Cronce et al (2007) developed the following equation relating the profiler-detected particle velocity of the smallest particles, V, to the vertical air motion (w) by

$$V = (\bar{u} + u')\sin\theta + \left(w + w' + V_{T_{min}}\right)\cos\theta, \quad (1)$$

where $\bar{u}$ is the horizontal wind, $u'$ and $w'$ are the turbulence due to wind shear in the horizontal and vertical directions, $V_{T_{min}}$ is the terminal velocity of the smallest particles, and θ is the half-beamwidth, which is 4.5° for the MIPS 915 MHz profiler. Solving Eq. (1) for vertical air motion yields:

$$w = \frac{V - (\bar{u} + u')\sin\theta}{\cos\theta} - V_{T_{min}} - w' \,. \quad (2)$$

The contributions to V are illustrated graphically in Figure 4.2, which shows the effect of the profiler's beamwidth on the detected values. At the edge of the radar beam, a component of the particles' horizontal motion is detected by the profiler in addition to the vertical component of motion. In keeping with the goal of a conservative (low) estimate of the vertical air motion, Eq. (1) assumes that the entire return echo from the particles comes from the edge of the beam.

The profiler data were filtered for noise with a simple signal-to-noise (SNR) ratio and spectrum width threshold filter. Data with SNR <-5 dB and a spectrum width < 1 $ms^{-1}$ were removed. These values were chosen such that almost all of the noise was filtered out while eliminating as little precipitation echo as possible. The *w* was determined for every range gate remaining that was at least 1 km above the melting level to ensure the sample volume was composed mainly of ice particles. The melting level was estimated as the 0°C level of a sounding from the RUC analyses before 1137 UTC, the first sounding launch time.

A complete wind analysis was performed for all times and range gates where spectra were recorded in order to produce values for $\overline{u}$, $u'$, and $w'$. The highest temporal resolution wind ($\overline{u}$) data are the wind profiler consensus winds, which are averaged over 30 minutes, so at times and locations where these were available, they were used. For gates where profiler winds were not available due to insufficient signal in one or more beams, rawinsonde winds were used. If neither source was available, hourly RUC soundings at the profiler sites were used. All three wind sources were linearly interpolated in height and time to provide profiles every 40 sec with 108 m vertical resolution. The turbulence, *u'*, was calculated with the relationship $u' = (\partial u/\partial z)(\Delta z/2)$, where $\Delta z$ is the gate spacing of the profiler data. For *w'*, the assumption was made that the horizontal turbulence scales with the vertical turbulence, or $w' = u'$ (Rogers et al. 1996).

To determine $V_{T_{min}}$, the diameter of the smallest particles measured by the profiler, $D_{min}$, must be known. To determine $D_{min}$, the reflectivity-weighted contribution of particles to the terminal velocity, $V_t(D)$ was first calculated. The diameter where $V_t(D)$ becomes appreciably greater than zero is $D_{min}$. Size distributions measured at several altitudes from PLOWS IOP 19 (14-15 February 2010; no aircraft measurements are available for year one of PLOWS) to calculate $V_t(D)$. The altitudes of these flight legs are illustrated graphically in Figure 4.3. These size distributions were created using the 2-DC probe for diameters less than 1.5375 mm and the 2-DP for diameters greater than that. The terminal velocity was then determined by using the Locatelli and Hobbs (1974) V-D relationship for side plane-type aggregates, $V_O = 0.82D^{0.12}$. Examination of the particle images from the 2-D probes show quite a few of these crystals present in the clouds sampled; also, the other velocity-diameter relationships given in the paper for other types of ice crystals produced similar terminal velocities.

These velocities were adjusted with the density correction factor from Foote and du Toit (1969), $V_T(D) = V_O(D)(\rho/\rho_O)^{0.4}$. The densities were calculated from interpolated rawinsonde measurements,

and at times and heights where rawinsonde data were not available, RUC soundings were used. An example of how this was determined is shown in Figure 4.4. The value where this occurred was determined graphically by noting where the magnitude of $V_t(D)$ abruptly jumped up from near zero. This threshold was also intentionally biased toward choosing a larger diameter minimum detectible particle in order to bias toward an underestimate of vertical air motion.

The uncertainty in the derived value for w was estimated using Eq. (7) from Cronce et al. (2007). For this study, $\Delta V$ is 0.14 $ms^{-1}$,which is half of a spectral bin width; the mean wind uncertainty $\Delta\bar{u}$ is the instrument error for the profiler and rawinsondes, 1 $ms^{-1}$, with the turbulence uncertainties $\Delta u'$ and $\Delta w'$ having a magnitude of twice that, or 2 $ms^{-1}$. The uncertainty in the beamwidth, $\Delta\theta$, is assumed to be 1°, and the uncertainty in the terminal velocity measurement is assumed to be 0.1 $ms^{-1}$ to ensure that any variations in fall speed due to particle habit are well within the uncertainty values, which were around 1 $ms^{-1}$.

### *4.2 Results for IOP-1*

The profiler measures a radial velocity moment. However, these data represent the radial total particle motions and must have the particle terminal velocity removed in order to ascertain the vertical air motions. For the LBM, the wind field is needed to remove the horizontal wind component and the horizontal and vertical turbulent components detected by the profiler. The combined wind analysis created to do this is presented in Figure 4.5, with the source of the values in Figure 4.6. This analysis was created primarily from the MIPS profiler, as winds could be calculated for most of the gates where the vertical beam had sufficient SNR and SW that they were not filtered. Most of the holes in the profiler data were filled in with data from the soundings. These two observed sources provided the vast

majority of the ingested winds; only a few remaining gates were outside both datasets and were filled in with RUC data.

Solving Equation (2) for every recorded spectrum yielded the LBM estimated vertical air motion, *w*, shown in Figure 4.7. Data from below a line 1 km above the bright band has been removed to ensure the results are only for areas with ice particles. The LBM indicates that the warm frontal region has some areas around 1000 UTC with vertical air motion values above 1 $ms^{-1}$, but for the most part values were negative. Most of the negative values were small in magnitude with values above -1 $ms^{-1}$, with the most negative values on the edges of the precipitation region reaching magnitudes of -2 $ms^{-1}$. The uncertainty on velocities in this region is near 1 $ms^{-1}$, meaning the sign of vertical velocities in much of the warm frontal region is uncertain.

The wraparound region contained much larger values for vertical air motion where the large upward particle motion was located. The maximum vertical air motion on the edge of the dry slot was estimated to be over 6 $ms^{-1}$, with a many profiles between from 2000 to 2200 UTC above 4 km showing *w* in excess of 1 $ms^{-1}$. These updrafts have a large vertical extent, sometimes spanning over 3 km in depth and extending to near the echo tops. On the warm side of the largest updrafts at the dry slot interface, there are several areas of deep convection emerging into the dry slot with upward vertical velocities over 5 $ms^{-1}$. The rest of the wraparound region shows air velocities within a range of -1 to +1 $ms^{-1}$, with the largest downward velocities on the edge of the echo region. Uncertainties in the vertical velocities in the wraparound region are around 0.7 $ms^{-1}$.

### *4.3 Further Tests from IOP 10 (8-9 December 2009)*

Analysis performed on an additional case beyond the one presented above showed that the LBM has a serious issue when applied to the MIPS profiler. This issue was not obvious for IOP 1, for which all the development work was done. An example of this problem is shown in the MIPS Doppler spectrum in Figure 4.8. The secondary peaks flanking the main power peak in the Doppler spectrum are the result of the profiler's side lobes return to the profiler. These side lobes stick out to varying degrees from the main power peak, which makes the determination of the most positive true return in the spectrum difficult, if not impossible. In some of the spectra, the side lobes are distinct from the main power peak, and in others they are almost indistinguishable from the main power peak.

The effect of these side lobes is evident in the profiler's spectrum width from IOP 10, shown in Figure 4.9. The horizontal stripes across the plot of greater spectrum width are areas where the side lobes are being picked up further away from the main power peak, and the lower stripes of spectrum width are produced by the side lobes being integrated into the main power peak. Comparing the spectrum width plot to the profiler-derived winds, shown in Figure 4.10, shows that the stripes in the spectrum width match the layers of different wind speed regimes. This indicates that the appearance of side lobes has a wind speed dependence, but there's no way to know for sure what controls their appearance and no way to truly correct for their appearance. Since their existence prevents the confident determination of the most positive echo return in the Doppler spectrum, we conclude that the LBM cannot safely be used with the MIPS profiler.

*Chapter 4 Figures*

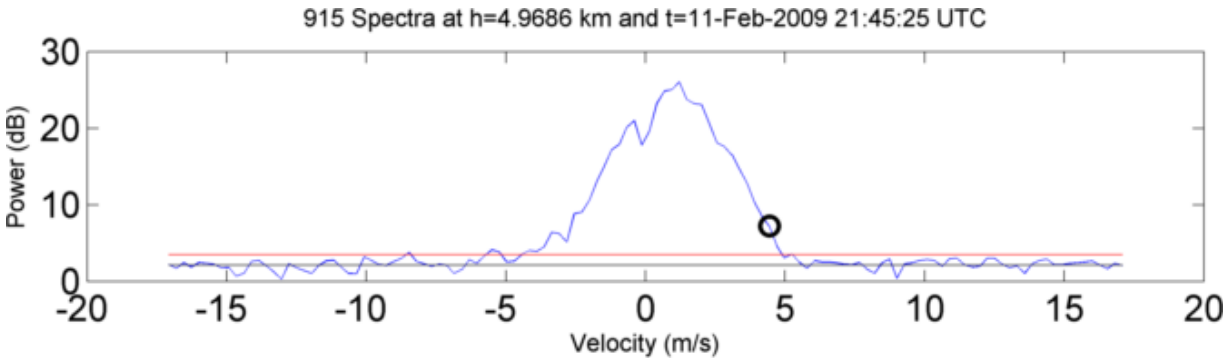


Figure 4.1: An example Doppler spectrum from the MIPS profiler. The black line indicates the noise floor, the red line three standard deviations above the noise floor, and the circle indicates the location of the signal of the smallest particles.

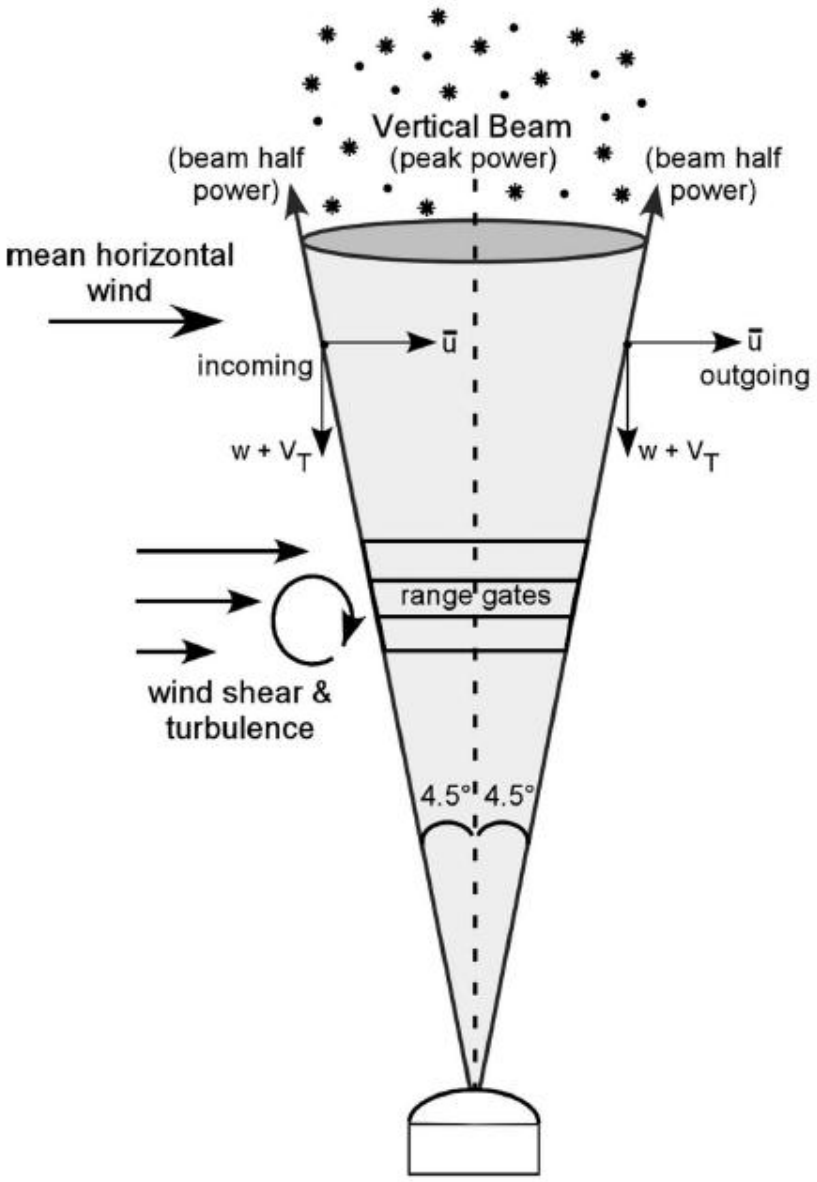


Figure 4.2: Schematic illustrating the various components of motion being detected by the profiler. From Cronce et al. (2007)

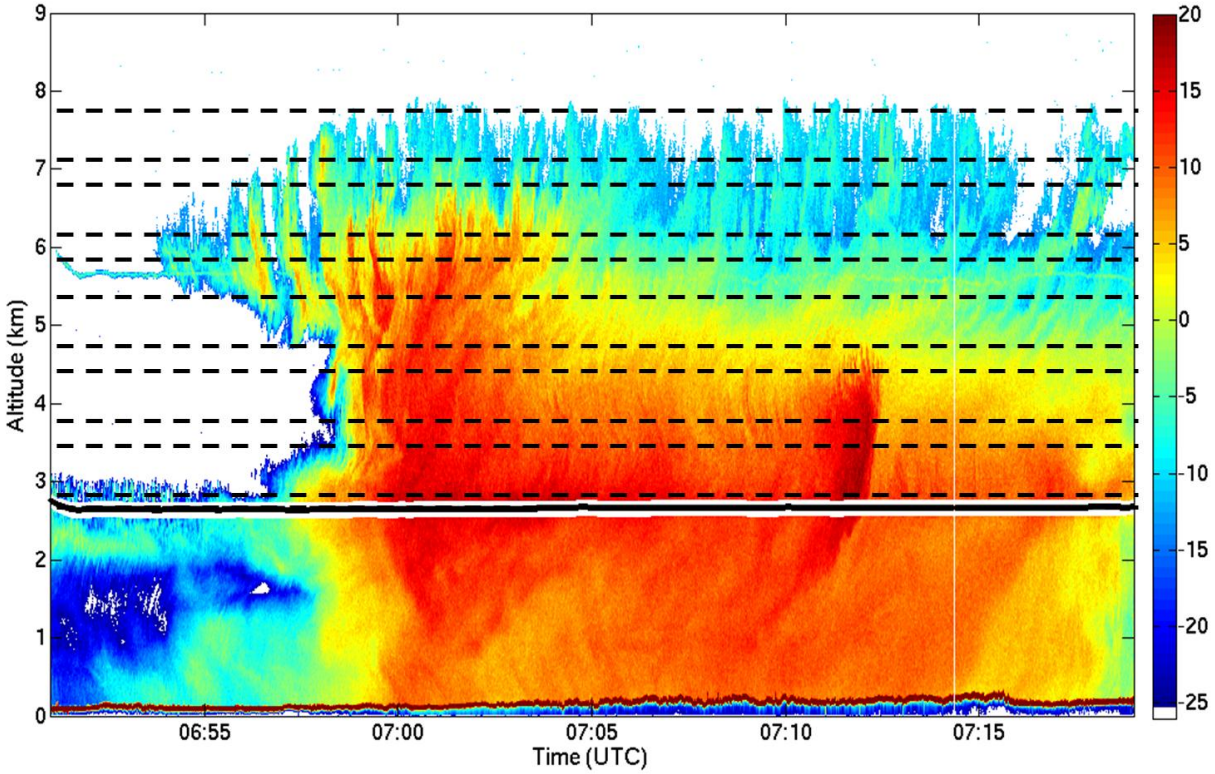


Figure 4.3: WCR radar reflectivity from IOP 19 with the altitudes of passes made by the NSF/NCAR C-130 indicated by dashed lines. These flight legs are the elevations where the size distributions were averaged for the LBM calculation.

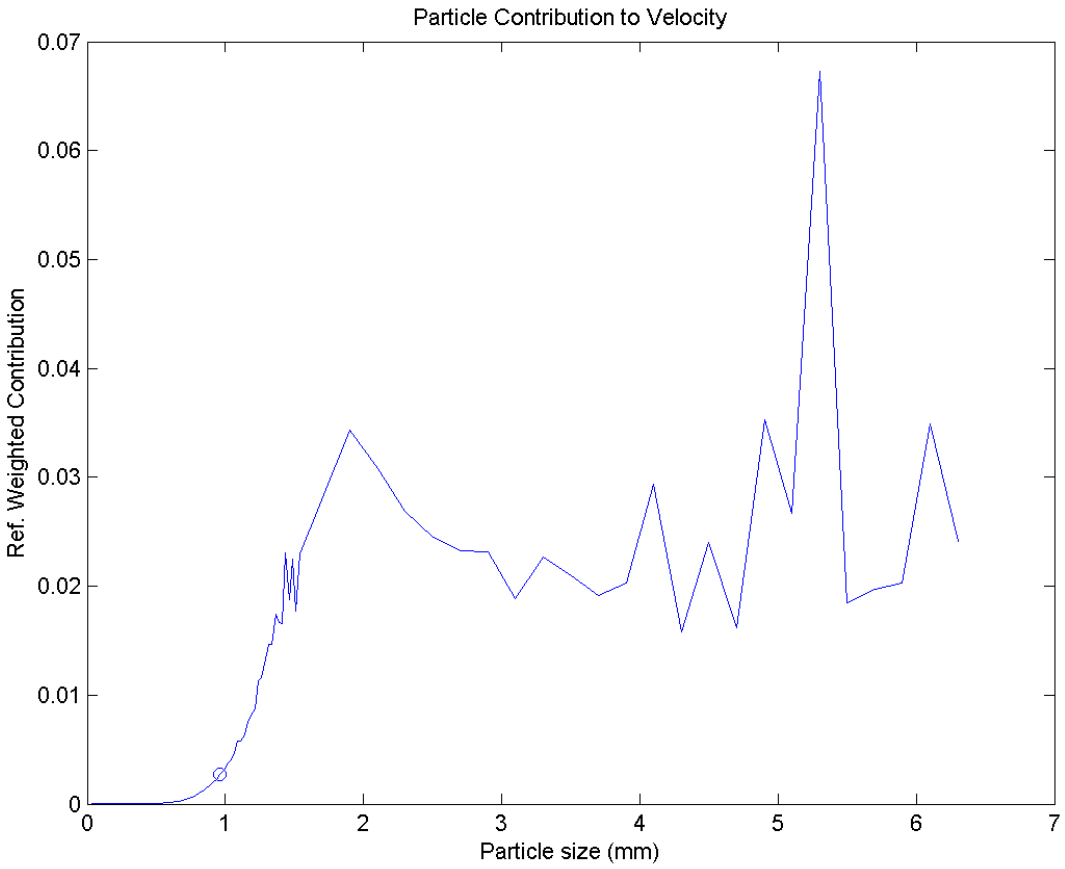


Figure 4.4: Plots of reflectivity-weighted contribution of particles to the terminal velocity. The circle indicates the diameter used for the smallest particles, determined by noting the location where the curve leaves the x-axis. This data was taken from PLOWS IOP 19.

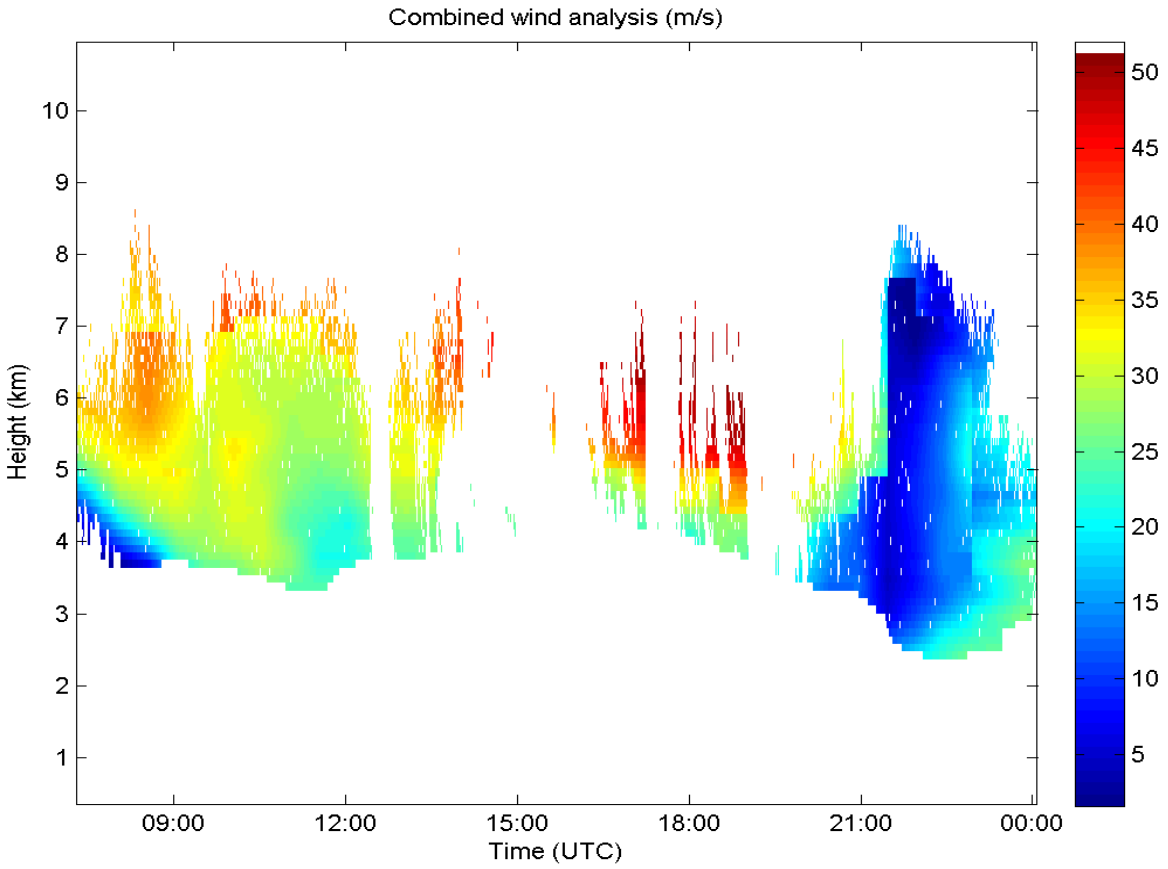


Figure 4.5: Combined wind analysis at every gate for IOP 1 where a spectrum was evaluated in $ms^{-1}$.

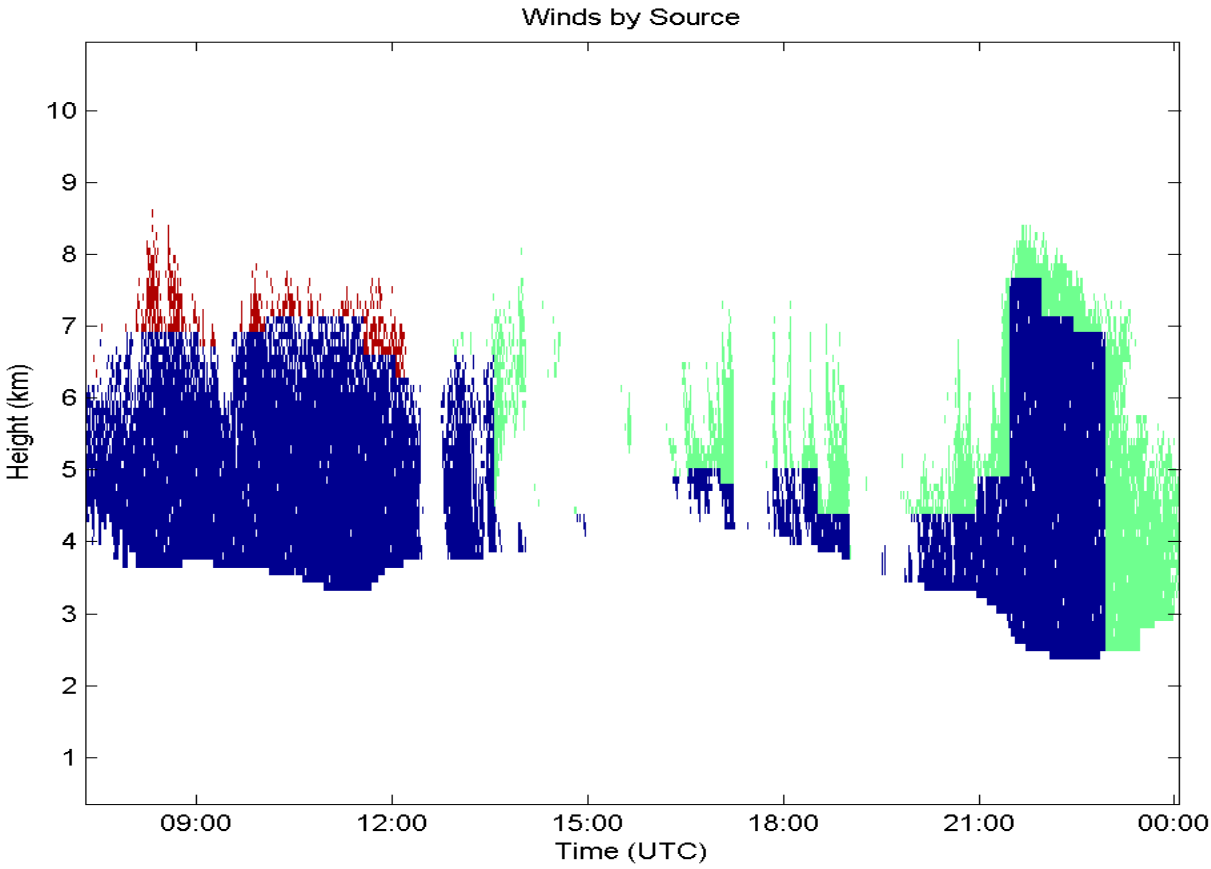


Figure 4.6: Mask indicating sources for the IOP 1 wind measurements in (a). Dark blue indicates MIPS profiler, light green indicates rawinsondes, deep red indicates RUC.

a)

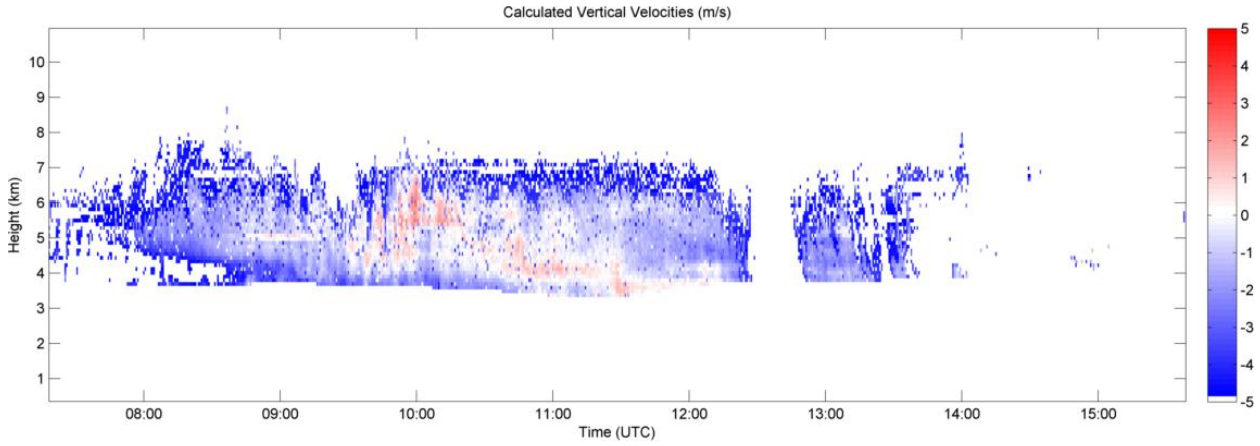


b)

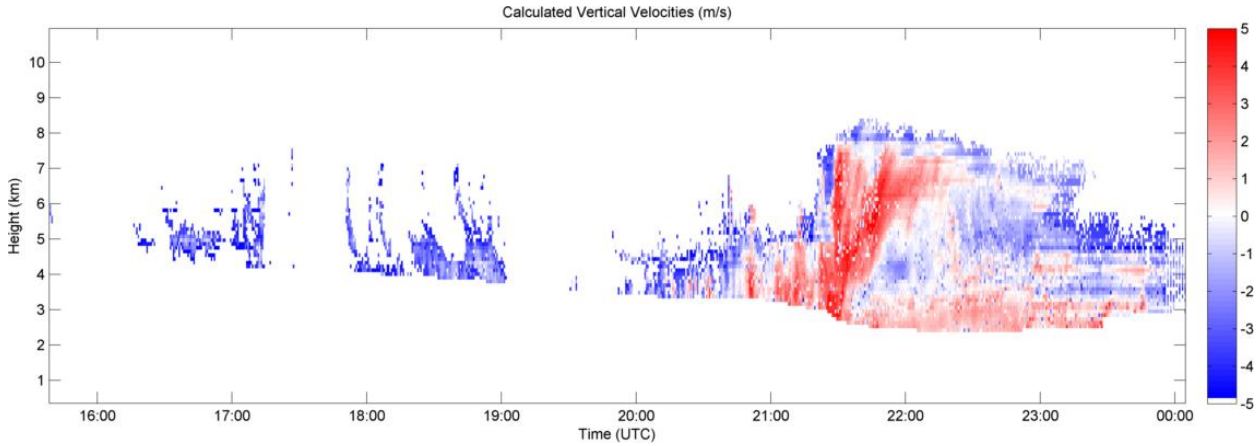


Figure 4.7: Calculated vertical air motion ($w$) values in $ms^{-1}$. Values are only presented for areas with ice particles. a) and b) are as in Figure 3.4.

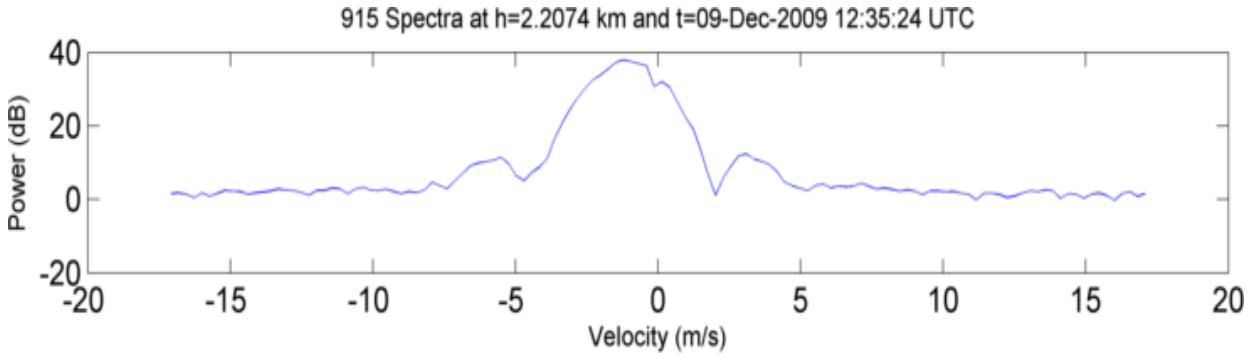


Figure 4.8: Example Doppler spectrum showing the appearance of side lobes flanking the main power return from the MIPS profiler from IOP 10.

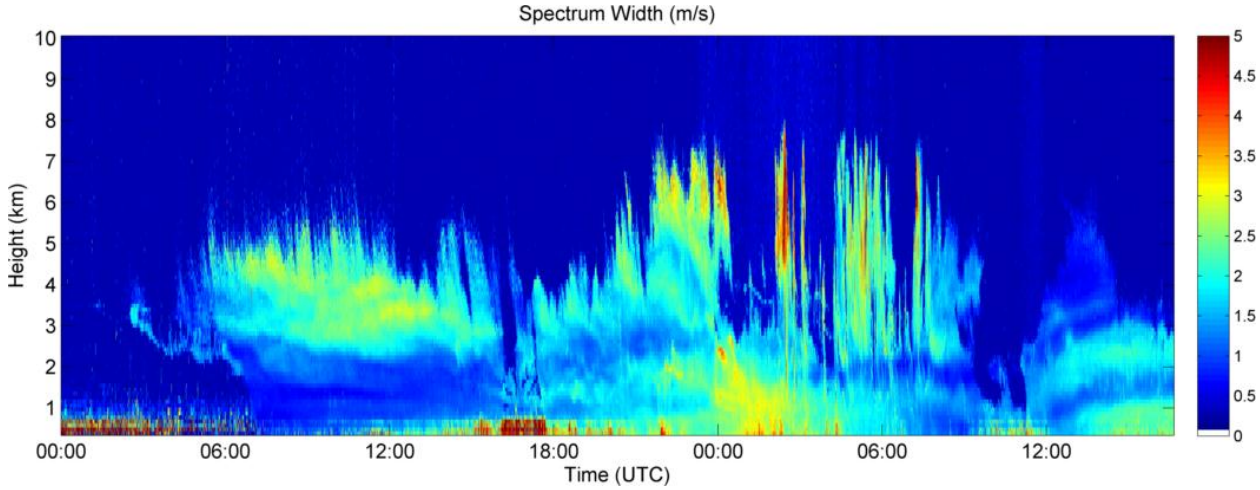


Figure 4.9: MIPS spectral width data for the PLOWS IOP 10 cyclone in $ms^{-1}$.

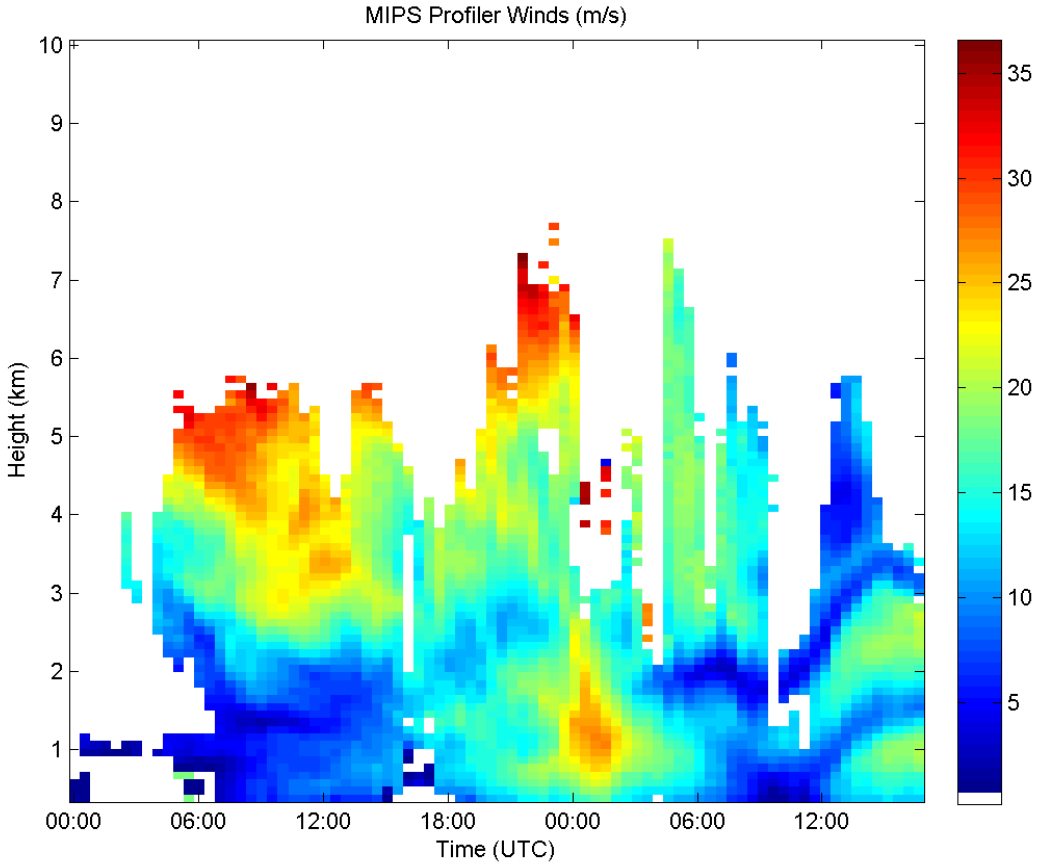


Figure 4.10: MIPS profiler calculated wind speeds for IOP 10 in $ms^{-1}$.

## 5. Radial Velocity Correction Method

### *5.1 Methodology*

This section describes an alternative method to derive vertical motions from the MIPS wind profiler. This method uses the radial velocity recorded by the MIPS profiler. Because this moment represents the peak of the Doppler spectrum, it is not susceptible to the side lobe issues that are a problem for the LBM. As for the LBM, this analysis was only done where the particle type was predominantly ice, with the same cutoff of 1 km above the bright band.

The radial velocity reported by the profiler, *V*, represents the total particle motion, which is a combination of the mean ensemble particle terminal velocity and the vertical air motion, *w*. The vertical motion is thus given by:

$$w = V - \bar{V}_T$$

where $\overline{V_T}$ is the mean ensemble particle terminal velocity adjusted for density following Foote and DuToit (1964). Velocities are again defined such that upward motion (away from the profiler) is positive, so the terminal velocity values are negative. This makes the calculated vertical air motions greater than the profiler radial velocities.

The mean ensemble particle terminal velocity $\bar{V}_T$ (uncorrected for density) was obtained by weighting the size distributions obtained from the two-dimensional probes during PLOWS IOP 19 by the sixth moment, equivalently the reflectivity, given by:

$$\bar{V}_T = \frac{\sum_{i=1}^{M} V_T(D_i) n(D_i) {D_i}^6 \Delta D_i}{\sum_{i=1}^{M} n(D_i) {D_i}^6 \Delta D_i}$$

where $V_T(D_i)$ is the terminal velocity of a particle with maximum dimension $D_i$, $n(D_i)$ is the number concentration at $D_i$, $D_i$ is the maximum dimension of a particle image, and $\Delta D_i$ is the width of the size bin. The size distributions were calculated the same way as they were for the LBM.

Figure 5.1 shows $\overline{V_T}$ as obtained from the Locatelli and Hobbs (1974) relationship for aggregates of side-planes as a function of altitude where the average size distribution measured during all flight legs was used in the calculation. The side-plane relationship was used since there were side plane aggregates in many of the flight legs, and many of the Locatelli and Hobbs relationships do not differ in magnitude by a significant amount. A flight leg during PLOWS was a constant altitude and direction pass through a system, and each point in Figure 5.1 represents the average taken through time for each of these flight legs. The average $\overline{V_T}$ of all the flight legs was 0.8±0.06 $ms^{-1}$. Utilizing a constant $\overline{V_T}$ of 0.8 $ms^{-1}$ for all altitudes should not introduce a significant error because there are larger uncertainties associated with a particle habit-terminal velocity relationship.

The $\overline{V_T}$ value of 0.8 $ms^{-1}$ was then corrected for density using the Foote and DuToit adjustment, leading to the final profile of $\overline{V_T}$ appearing in Fig. 5.2. Density values in this profile were added to each measurement of radial velocity to determine a final estimate for *w*.

### *5.2 Results*

As for the analysis with the lower bound method, the IOP 1 storm will be divided into two sections for examination, the warm frontal region and the wraparound region. The radial velocities associated with the wraparound region are shown in Figure 3.2. Using the terminal velocity method, these radial velocities were used to determine the vertical velocities, shown in Figure 5.3. The largest upward (positive) velocities are located near the echo tops, generally within 1-2 km of the top. The

profiles having upward motion greater than 3 $ms^{-1}$ between 2120 and 2200 UTC occur on the dry slot and wraparound interface. These updrafts span 3 km in depth, with smaller 1-2 km updrafts located toward the warm side of the wraparound before 2130 UTC. Only one significant downdraft appears near echo top, at 2120 UTC on the dry slot edge with a magnitude of 2 $ms^{-1}$. The rest of the calculated vertical motions after 2200 UTC were near zero to slightly downward.

Figure 5.4 shows the corresponding analysis for the warm frontal region. For comparison, the radial velocities were shown in Figure 3.2b. Just as with the wraparound region, the positive upward velocities are located again within 1-2 km of the echo tops. In general, the magnitudes are much smaller than the upward velocities in the wraparound region with the maxima only reaching around 3 $ms^{-1}$, and occurring less frequently over a smaller range of altitudes. Most of the upward velocities were less than 2 $ms^{-1}$. Heights further below the echo tops again show near zero or slightly downward values for vertical velocity. As shown in Chapter 2, the profiler does not sense the tops of these systems, so it is likely that these are not indicative of the velocity structure at cloud top.

Overall, the analyzed vertical motions provided a consistent picture in the February 11-12 cyclone. The upward vertical velocities throughout the storm are found near cloud top in both the warm frontal and wraparound regions. The magnitudes of the vertical velocities were larger in the wraparound region and the temporal scale of the updrafts was also larger in the wraparound region than in the warm frontal shield.

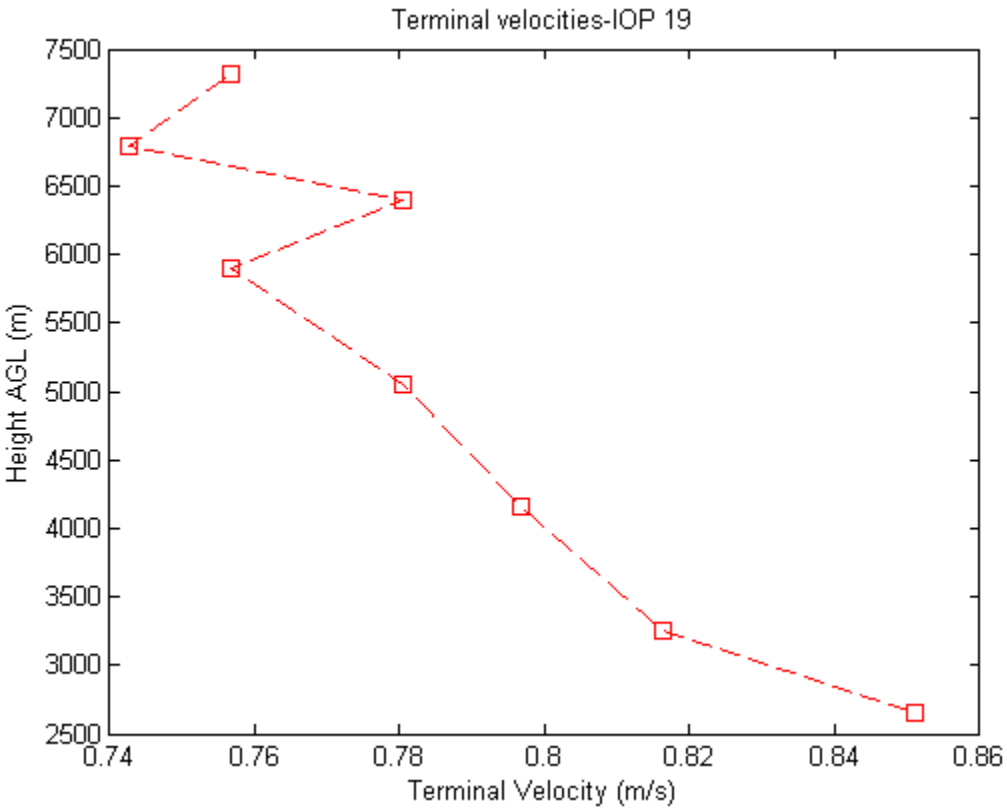


Figure 5.1: Reflectivity weighted terminal velocities for each flight leg in IOP 19.

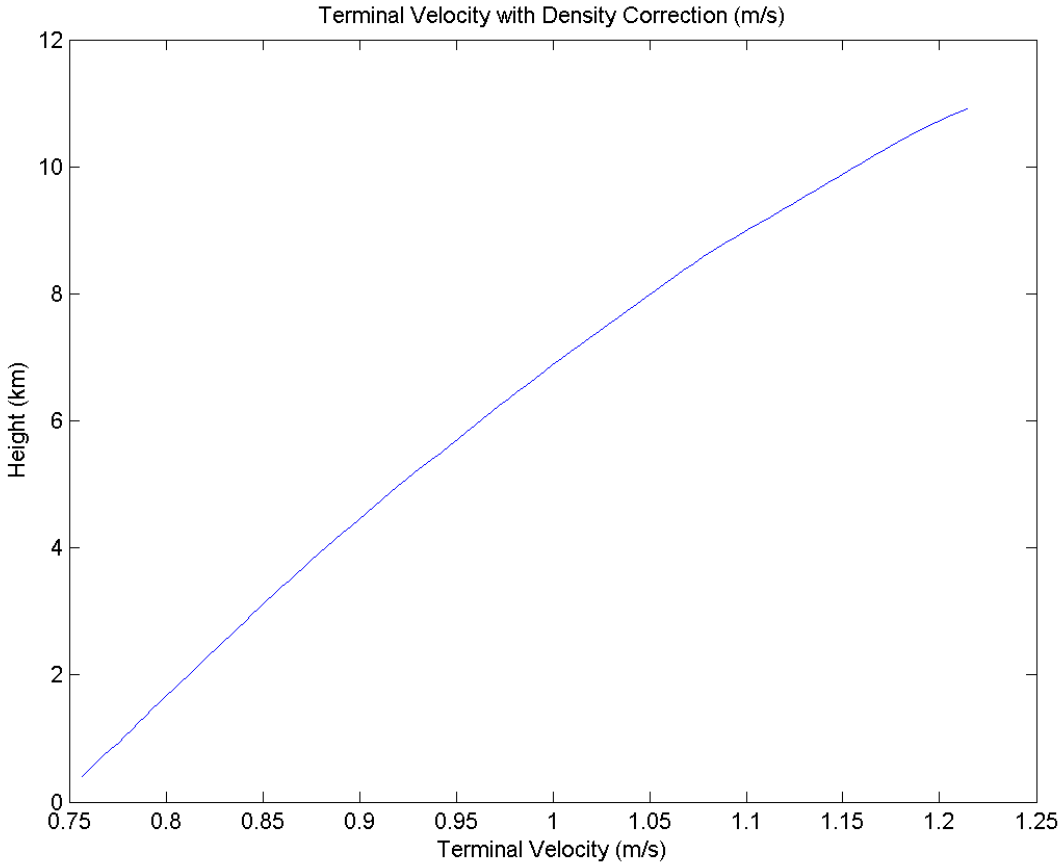


Figure 5.2: Terminal velocity profile utilized for this method, obtained by adjusting the averaged 0.8 $ms^{-1}$ terminal velocity values for the effects of density.

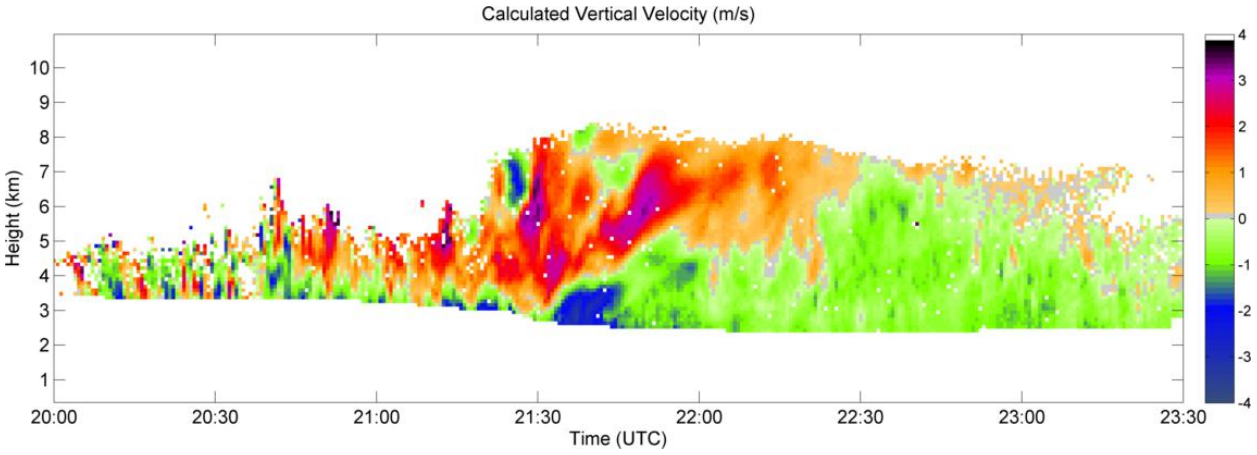


Figure 5.3: Vertical motions calculated from radial velocities for the wraparound region. Positive values indicate upward motion.

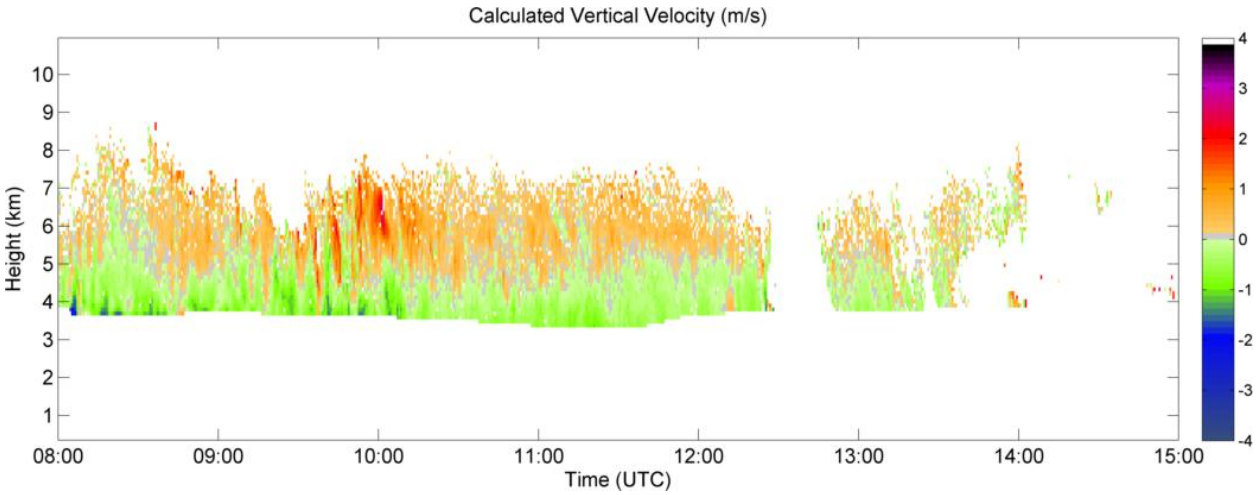


Figure 5.4: Same as Figure 5.3, but for the warm frontal region.

## 6. RUC Comparison

In order to provide an explanation of the vertical motions derived previously, the vertical motions were compared to data from the operational Rapid Update Cycle (RUC) model run by NCEP at a 20 km horizontal resolution. To assess the stability of the atmosphere, a time-section of RUC data was overlaid on top of the derived vertical air motions. To do this, vertical profiles of thermodynamic variables were generated over the profiler site using RUC gridded data, and these variables were used to calculate equivalent potential temperature with respect to ice ($\theta_{ei}$). $\theta_{ei}$ is calculated from the following relationship:

$$\theta_{ei} = \theta \exp \frac{L_f w_{si}}{c_p T_{LSL}}$$

where θ is the potential temperature, $L_f$ is the latent heat of fusion, $w_{si}$ is the saturation mixing ratio with respect to ice, $c_p$ is the specific heat of dry air at constant pressure, and $T_{LSL}$ is the temperature of the lifting sublimation level. The RUC vertical profiles are taken from the operational 20 km NCEP RUC, initialized the hour before the cross-section starts and interpolated from the nearest grid points to the profiler location.

The $\theta_{ei}$ analysis for the warm frontal region is contoured over the radial velocity derived vertical motions in Figure 6.1. Overall, the warm frontal region was analyzed to be relatively stable with $\theta_{ei}$ increasing with height in most areas. This agrees well with the relatively low magnitude vertical motions calculated as well as the smaller coverage of the updrafts. The stability lessens near echo top, where the updrafts were found. Because of the RUC model's relatively coarse resolution, smaller scale instabilities such as those associated with generating cells at the cloud top would not be resolved, so the fact that the RUC presents a stable profile where the larger (>1 $ms^{-1}$) updrafts are calculated does not necessarily preclude cloud top convection.

The corresponding plot for the wraparound region is shown in Figure 6.2. The wraparound region has larger vertical updrafts in size and magnitude than the warm frontal region, and this is also borne out by the stability analysis. In the wraparound region, the RUC indicates a large region between 2000 and 2200 UTC where the atmosphere is potentially unstable. The horizontal temporal scale of the echo top updrafts increases from the start of the wraparound region at 2000 UTC to 2200 UTC as the convection becomes stronger as upward velocities increase from 1-2 $ms^{-1}$ to 3-4 $ms^{-1}$. The maxima in updrafts located in the deeper echoes and are found on the elevated dry slot boundary from 2115 to 2200 UTC between 5 and 7 km. This increase in vertical motions is consistent with the stability analysis, as this whole region is potentially unstable, and the depth of the neutrally stable to unstable layer grows from 2 km at 2000 UTC to almost 4 km around 2330 UTC. The weakening in upward velocities to near zero after 2200 UTC is also consistent with the RUC equivalent potential temperature analysis which shows more stable conditions further from the elevated dry slot. Overall, the vertical orientation and magnitudes of the updrafts are consistent with upright potential instability release on the warm side of the wraparound. Cloud top convection may have been present on the cold side, but the CFAD analysis presented in Chapter 2 indicates that the profiler could not detect these circulations, if they exist in this storm.

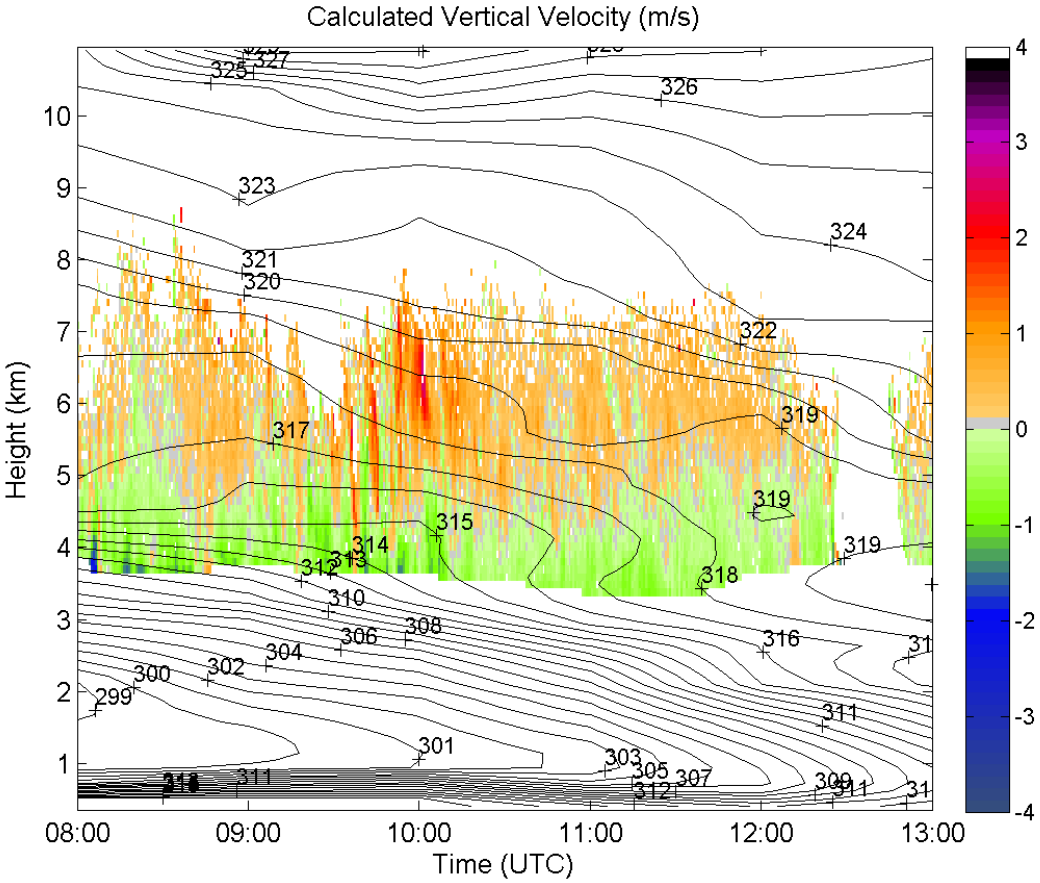


Figure 6.1: Calculated vertical velocities from the radial velocity method (Chapter 5) overlain with RUC equivalent potential temperature ($\theta_{ei}$) for the warm frontal region.

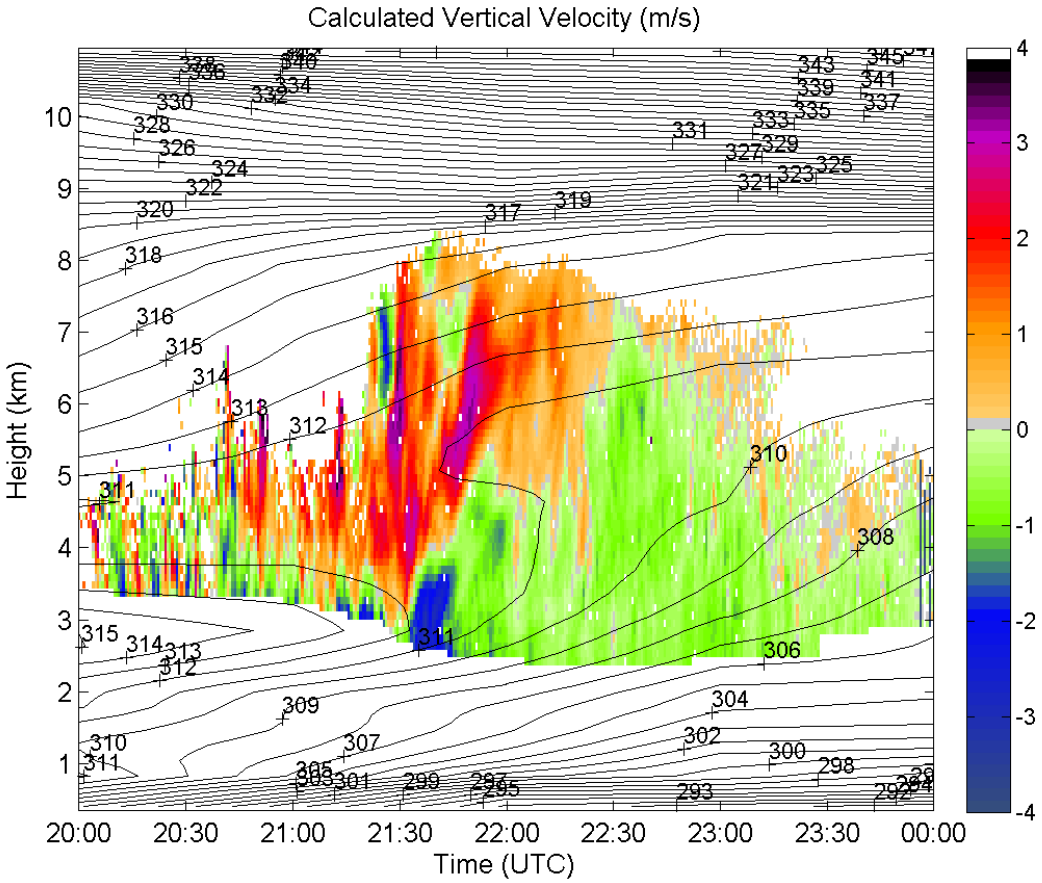


Figure 6.2: As with Figure 6.1, but for the wraparound region.

## 7. Conclusions

The goal of this project was an examination of methods to retrieve the vertical air velocity from the MIPS profiler in cyclones observed during PLOWS. Two methods were examined: the lower bound method (LBM), and removing the particle terminal velocities from the radial velocity using terminal velocity estimates from PLOWS microphysical measurements.

The Contoured Frequency by Altitude (CFAD) comparisons were useful for understanding the structure of the storms as well as for understanding how the radars, both the 915 MHz MIPS profiler and the W-band WCR, differ in observing wintertime cyclones. In studying continental cyclones from 2-3 December and 8-9 December 2009, CFADs from both radars show the same general behavior, with narrow distributions of around 1 $ms^{-1}$ radial velocity closer to the ground and spreading near cloud top. The CFADs on the warm side of the wraparound regions analyzed, where the atmosphere was potentially unstable, showed a deep layer 4-5 km deep of wider velocity distributions as well as velocities with the largest magnitudes, creating a spread in the distribution of 6+ $ms^{-1}$. On the cold side of the wraparound, the elevation range where the velocity spread was much smaller, encompassing only a narrow 1-2 km near cloud top. In addition, the spread in velocities is much narrower, with a spread of 2-3 $ms^{-1}$ instead of the 6+ $ms^{-1}$ spread in the CFADs on the warm side of the wraparound.

The CFADs from both radars tended to match well, especially given that they were not observing at the exact same time or location. The one noticeable difference in all of the comparisons was that the MIPS profiler did not show echoes that were as deep as the WCR. This difference suggests that the MIPS profiler and WCR are both capturing most of the storm well, but the profiler is not sensitive enough to detect particles within 1-2 km cloud top. As the prior analysis has shown that vertical motions can be quite strong at cloud top, it is important to keep this limitation of the MIPS profiler in mind when using

the system to study wintertime cyclones, particularly deep stratiform regions where the cloud tops may be convective and produce ice particles.

The LBM showed promising results with large positive upward velocities located on the warm side of the wraparound band of IOP 1. The largest upward air velocities were located on the edge of the dry slot-wraparound interface, with peak velocities of over 5 $ms^{-1}$. However, subsequent analysis of data from the IOP 10 case using the MIPS profiler showed side lobe contamination in the Doppler spectra. Since the LBM requires the values in the spectrum on the edges of the spectral peak and these values could be contaminated by side lobes, the values from the LBM calculations cannot be used with confidence.

Subtracting the particle terminal velocities from the radial velocity provides a better estimate of the vertical air velocities for the MIPS profiler since radial velocities are not contaminated by the side lobes. Microphysical measurements from PLOWS IOP 19 were used to arrive at a mean fall speed, which was corrected for density effects. The results of this method of deriving the vertical air motion fit well with the RUC equivalent potential temperature with respect to ice analysis, which was utilized to understand possible forcing mechanisms for these vertical motions. The larger positive values, from 1-3 $ms^{-1}$ were located in the less stable echo top region, and the largest values up to 6 $ms^{-1}$ were found where the RUC showed potential instability. The magnitudes of these vertical motions were largest on the edge of the wraparound region, with many regions of velocities greater than 1 $ms^{-1}$, which is consistent with the release of the potential instability. In the areas where the RUC indicated greater stability, calculated vertical motions were much less, with areas of strong stability showing near zero velocities.

**References**


Atlas, D., 1964: Advances in radar meteorology. *Advances in Geophysics,* Vol. 10, Academic Press, 318–478.

Bennetts, D. A., and B. J. Hoskins, 1979: Conditional symmetric instability—A possible explanation for frontal rainbands. *Quart. J. Roy. Meteor. Soc.,* **105,** 945–962.

Bennetts, D. A., and J. C. Sharp, 1982: The relevance of conditional symmetric instability to the prediction of mesoscale frontal rainbands. *Quart. J. Roy. Meteor. Soc.,* **108,** 595–602.

Bjerknes, J., and H. Solberg, 1922: Life cycle of cyclones and the polar front theory of atmospheric circulation. *Geofys. Publ.*, **3(1)**, 1 – 18.

Bluestein, H. B., 1993: *Synoptic-Dynamic Meteorology in Midlatitudes. Vol. 2, Observations and Theory of Weather Systems*. Oxford University Press, 594 pp.

Carbone, R., and A.R. Bohne, 1975: Cellular Snow Generation—A Doppler Radar Study. *J. Atmos. Sci.*, **32**, 1384–1394

Cronce M., R. M. Rauber, K. R. Knupp, B. F. Jewett, J. T. Walters, and D. Phillips 2007: Vertical motions in precipitation bands in three winter cyclones, *J. Appl. Meteor. and Clim*., **46**, 1523-1543.

Emanuel, K. A., 1983: The lagrangian parcel dynamics of moist symmetric instability. *J. Atmos. Sci.*, **40**, 2368-2376.

Foote, G. B., and P. S. du Toit, 1969: Terminal velocity of raindrops aloft. *J. Appl. Meteor.,* **8,** 249–253.

Hertzman O., and P. V. Hobbs, 1988: The mesoscale and microscale structure and organization of clouds and precipitation in midlatitude cyclones. Part XIV: Three dimensional airflow and vorticity budget of rainbands in a warm occlusion. *J. Atmos. Sci*., **45**, 893-914.

Hertzman O., P. V. Hobbs, and J. D. Locatelli, 1988: The mesoscale and microscale structure and organization of clouds and precipitation in midlatitude cyclones. Part XVI: Three dimensional airflow and vertical vorticity budget for a warm front. *J. Atmos. Sci*., **45**, 3650-3666.

Herzegh P. H., and P. V. Hobbs, 1980: The mesoscale and microscale structure and organization of clouds and precipitation in midlatitude cyclones. II: warm frontal clouds. J. Atmos. Sci., 37, 597-611.

Herzegh P. H., and P. V. Hobbs, 1981: The mesoscale and microscale structure and organization of clouds and precipitation in midlatitude cyclones. IV: Vertical air motions and microphysical structures of prefrontal surge clouds and cold frontal clouds. *J. Atmos. Sci.*, **38**, 1771-1784.

Hobbs, P.V., and J.D. Locatelli, 1978: Rainbands, Precipitation Cores and Generating Cells in a Cyclonic Storm. *J. Atmos. Sci.*, **35**, 230–241

Hobbs, P. V., T. J. Matejka, P. H. Herzegh, J. D. Locatelli, and R. A. Houze, Jr., 1980: The mesoscale and microscale structure and organization of clouds and precipitation in midlatitude cyclones. I: A case study of a cold front. *J. Atmos. Sci.*, **37**, 568-596.

Houze, R. A., Jr., S. A. Rutledge, T. J. Matejka, and P. V. Hobbs, 1981: The mesoscale and microscale structure and organization of clouds and precipitation in midlatitude cyclones. III: Air motions and precipitation growth in a warm frontal rainband. *J. Atmos. Sci*., **38**, 639-649.

Innocentini, V., and E. dos Santos Caetano Neto, 1992: A numerical study of the role of humidity in the updraft driven by moist slantwise convection. *J. Atmos. Sci*., **49**, 1092–1106.

Kreitzberg, C. W., and H. A. Brown, 1970:Mesoscale Weather Systems within an Occlusion. *J. Appl. Meteor*., **7**, 417–432.

Locatelli, J. D., and P. V. Hobbs, 1974: Fallspeeds and masses of solid precipitation particles. *J. Geophys. Res.,* **79,** 2185–2197.

Locatelli, J. D., and P. V. Hobbs, 1987: The mesoscale and microscale structure and organization of clouds and precipitation in midlatitude cyclones. XIII: Structure of a warm front. *J. Atmos. Sci*., **44**, 2290-2309.

Martin, J. E., 1998a: The structure and evolution of a continental winter cyclone. Part I: Frontal structure and the occlusion process. *Mon. Wea. Rev*., **126**, 303-328.

Martin, J. E., 1999: Quasigeostrophic forcing of ascent in the occluded sector of cyclones and the trowal airstream. *Mon. Wea. Rev*., **127**, 70-88.

Marshall, J.S., 1953: Precipitation trajectories and patterns. *J. Atmos. Sci.*, **10**, 25–29

Nicosia, D. J., and R. H. Grumm, 1999: Mesoscale band formation in three major northeastern United States snowstorms. *Wea. Forecasting*, **14**, 346-368.

Novak, D. R., L. F. Bosart, D. Keyser, and J. S. Waldstreicher, 2004: An observational study of cold season-banded precipitation in Northeast U.S. cyclones. *Wea. Forecasting*, **19**, 993-1010.

Persson, P. O. G., and T. T. Warner, 1995: The nonlinear evolution of idealized, unforced, conditional symmetric instability: a numerical study. *J. Atmos. Sci*., **52**, 3449-3474.

Probert-Jones, J. R., and W. G. Harper, 1961: Vertical air motions in showers as revealed by Doppler radar. *Proc. Ninth Weather Radar Conf.,* Boston, MA, Amer. Meteor. Soc., 225–232.

Rauber, R. M., M. K. Ramamurthy, and A. Tokay, 1994: Synoptic and mesoscale structure of a severe freezing rain event: The St. Valentine's Day ice storm. *Wea. Forecasting*, **9**, 183-208.

Reuter, G. W., and M. K. Yau, 1990: Observations of slantwise convective instability in winter cyclones. *Mon. Wea. Rev.,* **118,** 447–458.

Rogers, R. R., S. G. Leblanc, S. A. Cohn, W. L. Ecklund, D. A. Carter, and J. S. Wilson, 1996: Profiler measurements of turbulence and wind shear in a snowstorm. *Beitr. Phys. Freien Atmos.,* **69,** 27–36.

Sanders, F., 1986: Frontogenesis and symmetric stability in a major New England snowstorm. Mon. Wea. Rev., 114, 1847–1862.

Sanders, F., and L. F. Bosart, 1985: Mesoscale structure in the megalopolitan snowstorm, 11-12 February 1983. Part I: Frontogenetical forcing and symmetric instability. *J. Atmos. Sci*., **42**, 1050-1061.

Schultz, D. M., and P. N. Schumacher, 1999: The use and misuse of conditional symmetric instability. *Mon. Wea. Rev*., **127**, 2709-2732.

Schultz, D. M., and G. Vaughan, 2011: A Fresh Look at Conventional Wisdom. *Bull. Amer. Meteor. Soc.*, **92**, 443-466.

Seltzer, M. A., R. E. Passarelli, and K. A. Emanuel, 1985: The possible role of symmetric instability in the formation of precipitation bands. *J. Atmos. Sci*., **42**, 2207–2219.

Thorpe, A. J. and K. A. Emanuel, 1985: Frontogenesis in the presence of small stability to slantwise convection. J. Atmos. Sci., 42, 1809-1824.

Wang, P.-Y., and P. V. Hobbs, 1983: The mesoscale and microscale structure and organization of clouds and precipitation in midlatitude cyclones. X: Wavelike rainbands in an occlusion. *J. Atmos. Sci.,* **40,** 1950–1964.

Wang P-Y., D. B. Parsons, and P. V. Hobbs, 1983: The mesoscale and microscale structure and organization of clouds and precipitation in midlatitude cyclones. VI: Wavelike rainbands associated with a cold frontal zone. *J. Atmos. Sci*., **40**, 543-558.

Wexler, R., 1955: Radar analysis of precipitation streamers observed 25 February 1954. *J. Atmos. Sci.*, **12**, 391–393.

Wexler, R., and D. Atlas, 1959: Precipitation generating cells. *J. Atmos. Sci.*, **16**, 327–332

Wolfsberg, D. G., K. A. Emanuel, and R. E. Passarelli, 1986:Band formation in a New England winter storm. *Mon. Wea. Rev.,* **114,** 1552–1569.

Xu, Q., 1992: Formation and evolution of frontal rainbands and geostrophic potential vorticity anomalies. *J. Atmos. Sci*., **49**, 629-648.

Yuter, S.E., and R.A. Houze, 1995: Three-Dimensional Kinematic and Microphysical Evolution of Florida Cumulonimbus. Part II: Frequency Distributions of Vertical Velocity, Reflectivity, and Differential Reflectivity. *Mon. Wea. Rev.*, **123**, 1941–1963